

# TSD: An inverse problem approach for recovering the exoplanetary atmosphere transmission spectrum from high-resolution spectroscopy

NIKOLAI PISKUNOV <sup>1</sup>, ADAM D. RAINS <sup>1,2</sup> AND LINN BOLDT-CHRISTMAS <sup>1</sup>

<sup>1</sup>*Astronomy Division, Dept. of Physics and Astronomy, Uppsala University, Box 516, 75120 Uppsala, Sweden*

<sup>2</sup>*Instituto de Astrofísica, Pontificia Universidad Católica de Chile, Av. Vicuña Mackenna 4860, 782-0436 Macul, Santiago, Chile*

## ABSTRACT

Our ability to observe, detect, and characterize exoplanetary atmospheres has grown by leaps and bounds over the last 20 years, aided largely by developments in astronomical instrumentation; improvements in data analysis techniques; and an increase in the sophistication and availability of spectroscopic models. Over this time, detections have been made for a number of important molecular species across a range of wavelengths and spectral resolutions. Ground-based observations at high resolution are particularly valuable due to the high contrast achievable between the stellar spectral continuum and the cores of resolved exoplanet absorption features. However, the model-independent retrieval of such features remains a major hurdle in data analysis, with traditional methods being limited by both the choice of algorithm used to remove the non-exoplanetary components of the signal, as well as the accuracy of model template spectra used for cross-correlation. Here we present a new algorithm TSD (Transmission Spectroscopy Decomposition) formulated as an inverse problem in order to minimize the number of assumptions and theoretically modelled components included in the retrieval. Instead of cross-correlation with pre-computed template exoplanet spectra, we rely on high spectral resolution and instrument stability to distinguish between the stellar, exoplanetary, and telluric components and velocity frames in the sequence of absorption spectra taken during multiple transits. We demonstrate the performance of our new method using both simulated and real *K* band observations from ESO’s VLT/CRIRES+ instrument, and present results obtained from two transits of the highly-inflated super-Neptune WASP-107 b which orbits a nearby K7V star.

*Keywords:* Exoplanet atmospheres(484) — Transmission spectroscopy(2133) — High resolution spectroscopy(2096)

## 1. INTRODUCTION

Since the discovery of the first exoplanet orbiting a main sequence star, 51 Pegasi b, in 1995 (Mayor & Queloz 1995) astronomers have found almost 6 000 exoplanets<sup>1</sup> around various types of stars. The search for transiting systems in particular, where the planet can be seen to pass over the disk of its host star, has revealed itself as the most efficient planet detection technique and has been used to detect some  $\sim 70\%$  of all planets. Combined with radial velocity (RV) measurements, it also provides critical information about the size and mass of the planet, thus giving an estimate of the bulk density—the starting point for planet classification. Based on the bulk density, new types of planets not represented in the Solar System were found, like super-Earths with bulk densities similar to that of the Earth while  $\sim 3$ – $10$  times more massive, or mini-Neptunes with thick hydrogen-helium atmospheres but radii only  $\sim 2$ – $4$  Earth radii. At the time of its discovery, 51 Pegasi b was also considered an unusual planet, exemplifying the then-novel class of planets known as “hot Jupiters” that are not present in our Solar system but frequently found around solar-type stars.

Due to their large radii, short orbital periods, and high temperatures, hot Jupiters have been the focus of many space- and ground-based attempts to derive the physical properties of their atmospheres such as chemical composition, vertical temperature and pressure profiles (e.g. Sing et al. 2008; Birkby et al. 2013; Sedaghati et al. 2017; Boucher et al. 2021; Prinoth et al. 2022; Brogi et al. 2023; Tsai et al. 2023; Smith et al. 2024). These studies have broadly proceeded along

<sup>1</sup> See NASA Exoplanet Archive: [exoplanetarchive.ipac.caltech.edu](https://exoplanetarchive.ipac.caltech.edu).

two lines: time-series observations—often space-based—at high-photometric precision (but low-spectral resolution), or ground-based observations at high-spectral resolution from highly-stable ground-based instruments. For transmission<sup>2</sup> observations, both methods take advantage of the fact that during transit, part of the stellar flux is blocked by the planet including the outer semitransparent layers that compose its atmosphere. This transparency is a function of its chemical composition, thickness, temperature, pressure, and wavelength, and obtaining time-series data over a range of wavelengths simultaneously thus may be sensitive to the properties of the planetary atmosphere.

Photometric or low spectral resolution observations compare the light curves of the transit in a number of spectral windows selected to match strong spectral features associated with particular species (e.g. band heads of  $\text{H}_2\text{O}$ ,  $\text{CH}_4$ , or other molecules expected to be abundant in exoplanetary atmospheres). At these resolutions individual exoplanetary absorption features are poorly-resolved, and while this does reduce the contrast between transparent wavelengths and those with strong absorption, the overall signal-to-noise ratio (S/N) is improved. The best results require high-precision instruments, and generally rely on the exceptionally-high-photometric stability of space-based telescopes where many exoplanets have been characterized by, for example, Hubble (e.g. Charbonneau et al. 2002, Vidal-Madjar et al. 2004, Pont et al. 2008, Deming et al. 2013, Kreidberg et al. 2015, Wakeford et al. 2017), Spitzer (e.g. Tinetti et al. 2007, Désert et al. 2009, Knutson et al. 2011, Cowan et al. 2012), and more recently JWST (e.g. Alderson et al. 2023, Rustamkulov et al. 2023, Dyrek et al. 2024, Ahrrer et al. 2025). Although this method of characterization can be done with ground-based facilities (e.g. Bean et al. 2010, Sing et al. 2011, Lendl et al. 2016) the best results are still achieved from space where observations are free from the variability or telluric contamination of Earth’s atmosphere. Such sensitivity may make this approach our best bet for the analysis of Earth analogues, but planets on shorter period orbits can be targeted for complementary observations from the ground. Importantly, the interpretation of results does require a grid of planetary atmosphere models for finding the best match to the observations.

One alternative method takes advantage of the high contrast provided by strong *resolved* atomic or molecular absorption lines to distinguish the star and planet via the now-resolved Doppler shifts induced by the planet’s orbital motion. This setup restricts the observations to high spectral resolution instruments only available (at present) on ground-based telescopes. It allows the use of the largest photon collecting power but also suffers from contamination by telluric features in the Earth’s atmosphere.<sup>3</sup> The high-resolution approach was pioneered by Snellen et al. (2010) and this method with some enhancements is actively used today for the analysis of the transmission spectroscopy data (see review by Snellen 2025). The core idea is that an observed transmission spectrum is composed of three main components—stellar, telluric, and exoplanetary—with the stellar and telluric signals being essentially static<sup>4</sup> in wavelength space while the exoplanet transmission spectrum shifts with the orbital motion of the planet. Assuming high enough spectral resolution<sup>5</sup> one can attempt to remove the stellar and telluric components but not the exoplanetary signal based on the assumption that stellar and telluric spectra only change in time but not in wavelength. The removal is typically done with an iterative detrending process, analogous to Principal Component Analysis (PCA)—most commonly the widely-used SYSREM algorithm (e.g. Tamuz et al. 2005, Birkby et al. 2013). The detrended spectra—or residuals—contain noise and the planetary signal following its orbital Doppler shift (therefore, it is important to have a reliable and accurate orbital solution from RV observations). Detection of chemical species in the planetary atmosphere is then achieved by performing cross-correlation with a synthetic transmission template spectrum and comparing the trace of cross-correlation peaks throughout the transit with the prediction of the orbital solution.

The two methods are complementary. The analysis of flux-calibrated spectrophotometry covers a large spectral range (often at wavelengths inaccessible from the ground) providing simultaneous information about many molecular species present in exoplanetary atmospheres. Critically, it also preserves the continuum information of the planet transmission spectrum—typically destroyed by the detrending algorithms used at high-resolution—which encodes important information about the temperature–pressure structure of the planet atmosphere. High-resolution spectroscopy, on the other hand, is capable of distinguishing molecular and *atomic* species that have lines in overlapping spectral intervals (given an adequate template for the cross-correlation step), enabling for relative abundance measurements.<sup>6</sup> Additionally, by resolving individual adsorption lines, as well as their shifts and shapes, observations at high-resolution are capable of probing the “weather” on these planets, observing phenomena like winds and day-night-side variations

<sup>2</sup> These objects are also highly-amenable to *emission* (i.e. dayside) observations, but we restrict ourselves to considering transmission observations only for the remainder of our work here.

<sup>3</sup> This can complicate and cause confusion during data analysis due to the fact that some of the strongest telluric species like  $\text{H}_2\text{O}$ ,  $\text{CO}$ , and  $\text{CO}_2$  are *also* key target species in exoplanet atmospheres.

<sup>4</sup> In practice, the stellar lines experience a small (of order  $\sim 10 \text{ m s}^{-1}$ ) RV shift due to changes in the barycentric velocity over the transit.

<sup>5</sup> For a typical hot Jupiter on a 5 day orbit at 0.05 AU distance from a host K-dwarf star the line-of-sight velocity changes during transit by as much as  $12 \text{ km s}^{-1}$ . Thus, the resolution should be significantly higher with corresponding requirements on instrument stability.

<sup>6</sup> For a good summary of these advantages—and challenges—see the introduction of Brogi & Line 2019.

(e.g. Snellen et al. 2010; Brogi et al. 2016; Seidel et al. 2021; Gandhi et al. 2023; Cont et al. 2024; Seidel et al. 2025; Nortmann et al. 2025). Both methods share a common limitation in using models already at the signal detection phase where the adequacy of the models and the coverage of the parameter space are not easy to assess, raising questions about uncertainties of parameter determination (see e.g. Savel et al. 2025 and discussion within).

Switching focus back to the high-resolution technique, using detrending before the extraction of the exoplanet transmission signal with cross-correlation has its own limitations. These include the destruction of the exoplanet continuum (important for non-degenerate determination of the exoplanet atmospheric temperature-pressure profile, e.g. de Kok et al. 2013); a sensitivity to the accuracy and completeness of line lists used in template generation (e.g. Hoeijmakers et al. 2015, Brogi et al. 2017, Brogi & Line 2019, Gandhi et al. 2020); the inability to combine separate transits until after cross-correlation (i.e. *after* models have been introduced into the analysis, principally due to different barycentric velocities, but also inter-night instrumental or weather variations); the fact that detrending methods do not naturally ‘converge’ and thus require some sort of statistical metrics, simulations, or injection tests to determine the optimal number of iterations or components to remove<sup>7</sup> (e.g. Cheverall et al. 2023, Maguire et al. 2024); the potentially critical influence of seemingly separate decisions made for observations and data reduction, like observational cadence (e.g. Boldt-Christmas et al. 2024), spectral normalization, or pixel weighting on resulting detection; and—perhaps most critically—that detrending also destroys at least part of the planetary signal (e.g. Birkby et al. 2017, Meech et al. 2022). This approach has been successfully applied to many planets for the better part of the last 15 years, but we feel that it is time to consider other analysis techniques such as forward or inverse models (e.g. Aronson & Waldén 2015, Blain et al. 2024), or Doppler tomography (e.g. Watson et al. 2019, Esparza-Borges et al. 2022) which might have complementary advantages and approach the problem from a different angle.

In this paper, we describe a new inverse method capable of extracting planetary transmission spectra from high-resolution transmission spectroscopy without the use of detrending algorithms or the reliance on theoretical exoplanet models in the signal detection phase. We build upon the inverse modelling work by Aronson & Waldén (2015) to develop a functional inverse problem framework and software code, capable of reliably extracting planetary transmission spectrum for cool transiting exoplanets as observed with ground-based high-resolution spectrographs. In our numerical experiments, we consider  $K$  band observations of our test system, the warm Neptune WASP-107 b, at realistic S/N as achievable by current generation instrumentation. We call the new method “Transmission Spectroscopy Decomposition” or TSD.<sup>8</sup> TSD takes advantage of high spectral resolution, wavelength stability, and multiple transits to distinguish between the stellar, telluric, and planetary components—completely independently of any theoretical or empirical templates. The paper is structured as follows: Section 2 introduces our new inverse method, Section 3 gives an overview of our simulated transmission spectra formalism which we use to demonstrate our model’s performance using simulated  $K$  band transmission spectra matching ESO’s VLT/CRIRES+ instrument; Section 4 describes our observational data and the results of testing our model on two real transits of WASP-107 b; and Section 5 contains our analysis of results, a discussion putting TSD in context with more traditional detrending methodologies, and conclusions to the paper.

## 2. FORWARD MODEL

In this Section, we will introduce the model  $M_{\lambda}^j$  of an observed high-resolution spectrum of a transiting system taken in orbital phase number  $j$ . The model involves stellar flux ( $F_{\lambda}^*$ ) diminished by a wavelength-dependent planet “shadow” ( $I_{\lambda}$ ), selectively absorbed by telluric features in Earth’s atmosphere with optical depth  $\tau_{\lambda}$ , and observed at airmass  $z$ . We also include scaling ( $S^j$ ) and offset ( $D^j$ ) terms accounting for the seeing conditions and data reduction respectively, and  $\lambda$  is the wavelength in the restframe of the spectrometer.

$$M_{\lambda}^j = \left[ F_{\lambda \cdot (1+\gamma_j)}^* - I_{\lambda \cdot (1+\beta_j)}^j \cdot P_{\lambda \cdot (1+\delta_j)}^j \right] \cdot e^{-\tau_{\lambda} \cdot z_j} \cdot S^j + D^j. \quad (1)$$

Here  $\gamma$ ,  $\beta$  and  $\delta$  are unitless Doppler factors defining the shift in wavelength of the stellar flux, the specific intensity originating from the area blocked by the planet, and the planet transmission from their corresponding restframes to the observer reference frame. We assume the velocity to be positive when directed away from the observer (red shift) and therefore:

<sup>7</sup> In practice the number of principal components to remove depends on wavelength (e.g. the location and strength of stellar, telluric, and exoplanet absorption features), the weather (e.g. humidity affecting the strength or variability of H<sub>2</sub>O lines, the timing of the transit itself (e.g. barycentric velocity and how close the telluric and stellar RV frames are), instrumental effects (e.g. time varying PSF or blaze), and the combination of star, planet, and species of interest (e.g. whether the star/tellurics/planet have species in common).

<sup>8</sup> Internally, TSD is also occasionally referred to as “TueSDay”.

- $\gamma_j = (v_{\text{bary}} + v_{\text{star}})/c$  is a barycentric + radial velocity Doppler shift factor for the star ( $c$  is the speed of light).
- $\beta_j = (v_{\text{bary}} + v_{\text{star}} + v \sin i \cdot x_{\text{planet}})/c$  differs from stellar velocity if the data resolves stellar rotation.  $x_{\text{planet}}$  is the distance between the projected planet position and the projection of the stellar rotation axis in units of the stellar radius.  $x_{\text{planet}}$  is negative for the hemisphere that moves toward the observer.  $v \sin i$  is the line-of-sight component of the equatorial stellar rotation. The underlying assumption of solid rotation can be (if necessary) generalized to include differential rotation.
- $\delta_j = (v_{\text{bary}} + v_{\text{star}} + v_{\text{planet}}^j)/c$  is the planet’s Doppler shift. In the simplest case of a circular orbit, the planetary component will be the line-of-sight component of the orbital velocity multiplied by the sine of the orbital phase  $j$  in radians.

The square bracket in Equation 1 contains the flux coming from the star in the direction of observer, and consists of the total stellar flux  $F$  minus the part that is blocked by the planet. The latter is proportional to the specific intensity radiated in the direction of the observer from the obscured part of the stellar surface. The proportionality coefficient  $P$  that we will call “the planet blocking function” is given by the ratio of radii squared  $(R_{\text{planet}}/R_{\star})^2$  where  $R_{\text{planet}}$  is the effective radius of the planet blocking all radiation at a given wavelength. For the case of an Earth-like planet, it can be understood as the radius of the planet surface plus the height of the atmosphere that is optically thick for the grazing rays at a given wavelength. For gas planets, no such distinction exists, but the value of  $P \geq 0$  in both cases. Atmospheric transmission is, of course, a function of wavelength and therefore the subject of Doppler shifts due to the orbital motion of the planet. For all the orbital phases where planetary footprint is fully inside the stellar disk, this Doppler shift is the only dependence on the orbital phase (assuming a spherically symmetric atmosphere).  $P_{\lambda \cdot \delta_j}^j$  changes dramatically as the planet crosses the stellar limb, and goes to zero outside the transit.

The exponential multiplier to the square bracket is the description of the Earth’s telluric absorption. Here,  $\tau_{\lambda}$  is the monochromatic optical path through the Earth atmosphere in the zenith direction (airmass unity) and  $z_j$  is the airmass of the target at every observed phase. The choice of optical path naturally constrains the telluric features to absorption, preventing instabilities in the inverse solver (see Section 2.1). Finally, the phase-dependent factor  $S^j$  and offset  $D^j$  are there to correct for variable observing conditions, mostly affected by the airmass, seeing, wind, slit losses and data reduction. Ideally, these vectors should be smooth function of the airmass/time but in real life this is seldom the case.

When writing Equation 1, we make a several simplifying assumptions. We assume that the stellar flux  $F$  and the planet blocking function  $P$  are constant in time (i.e. no phase dependence except for the ingress and egress, which are known from the orbital geometry), and the scaling factor  $S$  and offset  $D$  change with phase but are the same for all wavelengths. For different transits (i.e. nights), telluric absorption may vary, but for a single transit it does not change in time except due to the variable airmass  $z_j$ . Finally, we assume that the radial components of all velocities (telescope, star, planet, stellar rotation) are known for each phase *a priori*. These assumptions break down in the case of stellar activity or spots, exoplanet asymmetries or time and velocity resolved “weather”, or large Earth-humidity variations within a single night that would cause H<sub>2</sub>O telluric features to be time variable. We discuss the effect of these limitations further in Section 5.1.

With these assumptions, we can now list the unknown functions: stellar flux  $F$ , planet blocking function  $P$ , intensity scaling factor  $S$ , background offset  $D$ , and optical thickness of telluric absorption  $T$  for every transit. The inclusion of multiple transits is not just desirable. It is crucial for success: the changes of Doppler shift during a single transit are not sufficient to distinguish between the telluric and the stellar lines, thus creating a degeneracy. Change in barycentric correction *between* transits can shift stellar features sufficiently to remove this ambiguity.

### 2.1. Minimisation problem and unknown functions

The discrepancy function  $\Phi$  measures the differences between the model  $M_{\lambda}^j$  and the observations  $O_{\lambda}^j$ :

$$\Phi \equiv \sum_{\lambda, j} \omega_{\lambda}^j \left[ M_{\lambda}^j - O_{\lambda}^j \right]^2. \quad (2)$$

where  $\omega$  here are optional weighting terms for data points based on signal-to-noise ratio of observations. We note that the most important weight component—the telluric absorption—is naturally built into the definition of  $\Phi$ : the

wavelengths with strong telluric absorption will automatically have smaller contribution to  $\Phi$ . Now, we will attempt to reconstruct the unknown functions that minimizes  $\Phi$ .

$$\Phi = \min \quad (3)$$

To inform the sequence of our solving procedure described later in Section 2.4, it is useful to take a closer look at each of the unknown functions  $F$ ,  $P$ ,  $T$ ,  $S$ , and  $D$  before proceeding. The telluric absorption can be measured before and after the transit and then verified using interpolation into the phase and the airmass of individual transit spectra. For multiple transits, however, we cannot assume this function to be the same and so we must determine the telluric absorption vector for each transit separately. Similarly, spectra taken before and after the transit and corrected for telluric absorption can provide a good initial guess for the stellar flux spectrum  $F_\lambda$ . For the planetary blocking function  $P$ , we know that it is both positive and a function of wavelength, so a suitable initial guess could then be a constant value set to the squared ratio of the photometric planet and stellar radii. The scaling  $S^j$  and offset  $D^j$  vectors are a function of the orbital phase only and in this sense they are “orthogonal” to the flux, tellurics and planetary blocking function.

## 2.2. Specific intensity

The remaining unknown function is the specific intensity. To obtain  $I_\lambda^j$  we can rely on a model atmosphere and spectral synthesis for the star. Orbital phase  $j$  defines the limb distance parameter  $\mu$  on the stellar disk, at which the specific intensity should be computed, where  $\mu$  is the cosine of the angle between the local normal and the direction to the observer at the eclipsed part of the stellar surface. Thus, our procedure consists of the following steps:

1. Find fundamental parameters of the host star, e.g. using SME (Piskunov & Valenti 2017) with high-quality spectra and any other available non-spectroscopic constraints (asteroseismology, parallax, accurate photometry, etc.).
2. Verify that the derived parameters are capable of reproducing the observed spectrum in the wavelength range in which the transit data was taken.
3. Compute a model atmosphere with the derived parameters.
4. Compute flux spectra and repeat the tests in steps 1 and 2.
5. Compute  $\mu$  positions for all phases (i.e. exposures) during the transit where the planet’s shadow is fully or partially inside the stellar disk.
6. Compute synthetic specific intensities using the parameters, model, and  $\mu$  angles derived above.

Alternatively, a specific intensity can be derived from the flux using a limb-darkening law (e.g. Kostogryz et al. 2024, and the references within). The theory of stellar atmospheres predicts the intensity to be a smooth function of the limb distance  $\mu$ , frequently approximated with the following expression (Claret 2000):

$$I(\mu)/I(1) = 1 - \sum_{k=1}^K a_k \cdot (1 - \mu^{k/2}) = 1 - \sum_{k=1}^K a_k + \sum_{k=1}^K a_k \cdot \mu^{k/2}, \quad (4)$$

where  $a_k$  are the fitting coefficients. Typically truncating summation at  $K$  equal to 4 is considered sufficient to achieve better than 0.1% precision (Magic et al. 2015). Assuming a non-rotating star without any active regions, we can also compute the monochromatic flux by disk integrating the specific intensity:

$$F = 2\pi \int_0^1 I(\mu) \mu d\mu = \pi \cdot I(1) \cdot \left( 1 - \sum_{k=1}^K \frac{k \cdot a_k}{k+4} \right), \quad (5)$$

which gives us the relation between the flux and the central intensity. Now we can use the flux in Equation 4 instead of  $I(1)$ :

$$I(\mu) = F \cdot \left( 1 - \sum_{k=1}^K a_k + \sum_{k=1}^K a_k \cdot \mu^{k/2} \right) / \pi \cdot \left( 1 - \sum_{k=1}^K \frac{k \cdot a_k}{k+4} \right). \quad (6)$$

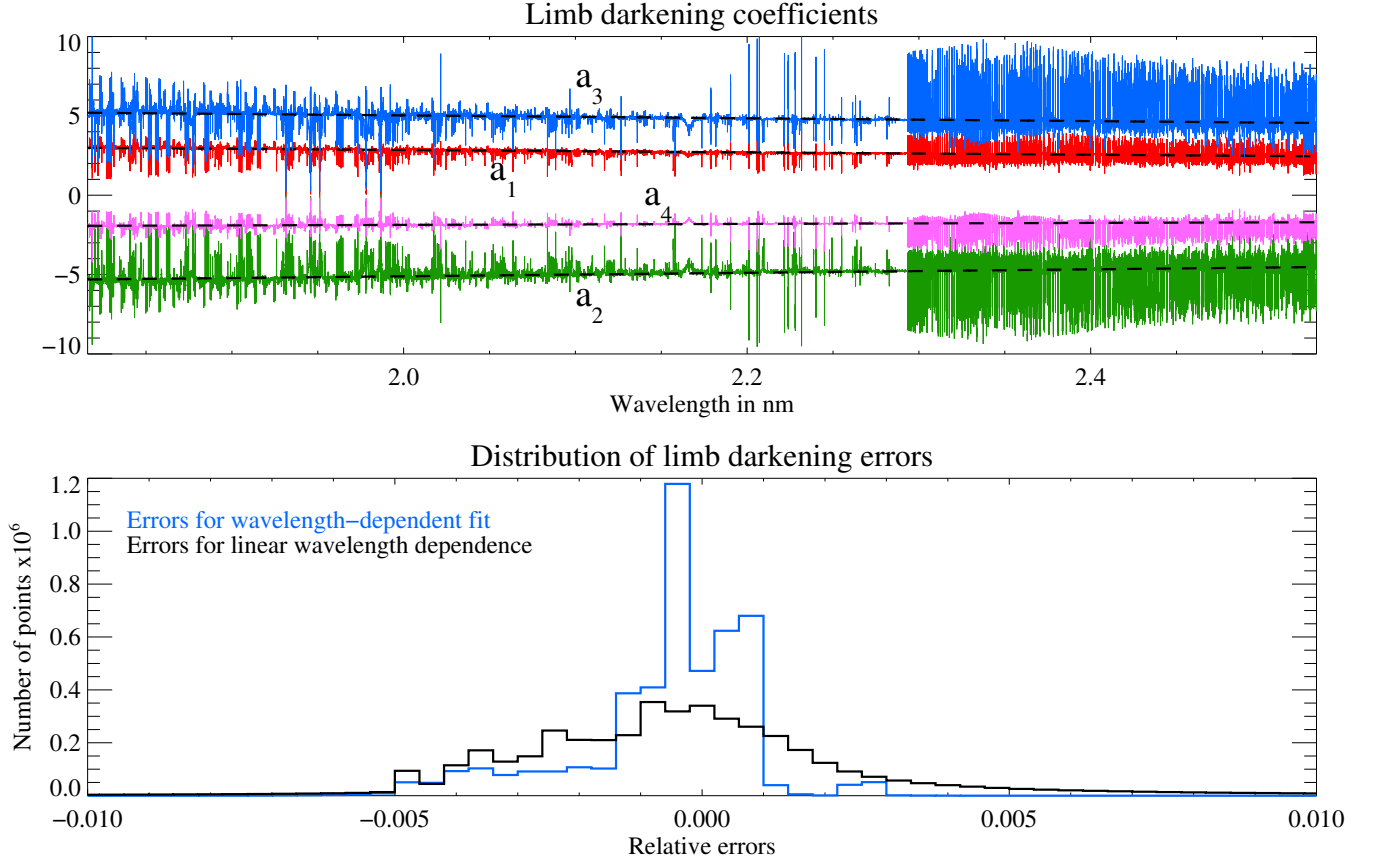


**Figure 1. Top:** Monochromatic limb darkening coefficients as in Equation 4 computed for specific intensities in the near-infrared using a MARCS model atmosphere (Gustafsson et al. 2008). The parameters of the model are the following:  $T_{\text{eff}} = 3340$  K,  $\log g = 5$ ,  $[\text{Fe}/\text{H}] = -0.34$ ,  $v_{\text{macro}} = 1 \text{ km s}^{-1}$ . Limb darkening was calculated for wavelength sampling at resolution  $R=100\,000$  and for 49 limb distances ( $\mu$  angles) with decreasing spacing toward the limb. Dashed black lines indicate the linear fit for each coefficient. **Bottom:** The distribution of relative errors when reconstructing specific intensities using wavelength-dependent limb darkening coefficients (in black) and their linear fit (in blue). In the first case all wavelength and disk points are reproduced to better than 1%. For the blue histogram 94% of points are reproduced to better than 1%.

Most of our targets are slow rotators, meaning that rotational broadening is not resolved by our observations and we can safely assume zero rotation. Under this assumption, the  $\gamma_j$  and  $\beta_j$  Doppler factors are identical, reducing the number of unique velocity frames when modeling these targets. Slow rotation is also statistically associated with a low level of magnetic activity (see e.g. Baliunas et al. 1996, Stelzer et al. 2016, Mittag et al. 2018), but it does not guarantee the absence of active regions along the transit trajectory.

Our aim here is to remove from the forward model the last unknown function that cannot be derived directly from observations. The advantage of using limb darkening as opposed to explicit calculation of specific intensity from model atmospheres is that the specific intensity is related to the observed flux, making it internally consistent. The downside is that the assumptions we make may hold for some systems but not for the others; however, slow rotation means that our observations do not resolve the rotational broadening of spectral lines. For example, for an instrument with resolving power  $R = 100\,000$ , stellar rotation  $v \sin i$  less than  $1.5 \text{ km s}^{-1}$  will not change the measured line profiles. This is a limiting factor of the method as currently implemented, but we will properly account for stellar rotation in future versions of TSD.

The remaining fundamental problem is that the limb-darkening coefficients  $a_k$  strongly depend on the opacity variation and thus on the wavelength. The coefficients could be determined empirically (i.e. as free parameters) or theoretically, but both methods have problems. If we were to empirically determine wavelength-dependent limb-darkening coefficients, we would risk ending up with a poorly constrained problem. On the other hand, model atmosphere-based coefficients are known not to perfectly match the reality of the Sun except when using 3D hydrodynamical models

(Magic et al. 2015). This is particularly true for the blue part of the spectrum and close to the solar limb. Still, even without a 3D model this approach gives a very good fit to specific intensities for most of the stellar disk and allows us to assess the wavelength dependence of the coefficients for individual targets. An example based on the parameters of the planet-host star WASP-107 is shown in Figure 1. The selected spectral interval in the  $K$  band is popular for high-resolution transmission spectroscopy of exoplanets because it contains spectral features of several interesting molecules, such as  $\text{H}_2\text{O}$ ,  $\text{CO}$ ,  $\text{CO}_2$ ,  $\text{NH}_3$ , and  $\text{CH}_4$ . The derived coefficients are strongly variable on a small scale (as shown by the color lines on the top panel of Figure 1), but because the summation components in Equation 6 are similar in magnitude and the odd and even coefficients have opposite signs, the wavelength dependence of the sum is largely reduced. In fact, accounting for the linear trend of the limb darkening coefficients already captures most of the effect. The distribution of relative errors between the specific intensities, computed from a MARCS atmospheric model (Gustafsson et al. 2008) and our approximation using  $K = 4$  shows that accounting for linear dependence brings the errors well below 1% for the majority (94%) of disk positions and wavelengths (bottom panel of Figure 1). This is only slightly worse than using the exact wavelength dependence of the limb darkening coefficients, and is comparable to the expected approximation accuracy of Equation 6 with  $K = 4$ . We note that larger deviations occur close to the limb where the planet spends only a small fraction of the transit.

Accepting linear wavelength dependence of the limb darkening coefficients, restricting the approximation to four terms, and introducing new notations for the nominator  $L$  and denominator  $N$  for ratio in the RHS of Equation 6 we can re-write our model without using specific intensity explicitly:

$$\begin{aligned} N_\lambda &= \pi \cdot \left[ 1 - \sum_{k=1}^4 \frac{k \cdot a(\lambda)_k}{k+4} \right], \\ L_{\lambda,j} &= 1 - \sum_{k=1}^4 a(\lambda)_k \cdot (1 - \mu_j^{k/2}), \\ M_\lambda^j &= \left[ F_{\lambda \cdot (1+\gamma_j)}^* - F_{\lambda \cdot (1+\beta_j)}^* \cdot \frac{L_{\lambda,j}}{N_\lambda} \cdot P_{\lambda \cdot (1+\delta_j)} \right] \cdot e^{-\tau_\lambda \cdot z_j} \cdot S^j + D^j. \end{aligned} \quad (7)$$

We selected not to apply Doppler shift to the limb-darkening components: the slope of the wavelength dependence in our spectral region is so small that for typical values of  $\gamma$  and  $\beta$  the relative changes to  $L$  and  $N$  are below  $10^{-7}$  and can be safely ignored.

### 2.3. Linearisation

From this point on, we assume that all observations are taken when the planet shadow is fully inside the stellar disk, and thus the planetary blocking function  $P$  is only a function of the wavelength and not of the orbital phase. This is only done to make the following algebra more transparent. In our TSD implementation, we account for such configurations by computing the fraction of the area  $P$  projected onto the stellar disk. However, this is only partly correct as the atmosphere becomes a variable transparency circle due to several factors (day- and night-side differences, atmospheric refraction, etc.), but we note that the partial eclipse phases are less sensitive to  $P$  and hence not crucial for recovery of the planet blocking function, making this an acceptable compromise.

As for any least-squares problem, to find the solution we take partial derivatives of  $\Phi$  over free parameters and then set it to 0. However, we have to be careful with the Doppler shifts. For the partial derivative over the wavelength-dependent function  $F^*$ ,  $P$ , and  $\tau$ , we need to shift the model into the restframe of the function we are solving for in order to get the derivative vector matching specific wavelength pixel. *This is the magic secret of making TSD work.*

The expressions for the derivatives are trivial for some unknown functions and less trivial for others. Here we write them out to have all the math for the reader (and the authors) in one place. Let's start with re-writing the expression for  $\Phi$  in the instrumental restframe:

$$M_\lambda^j = \left[ F_{\lambda \cdot (1+\gamma_j)}^* - I_{\lambda \cdot (1+\beta_j)}^j \cdot P_\lambda \right] \cdot e^{-\tau_\lambda \cdot z_j} \cdot S^j + D^j \quad (8)$$

$$\Phi = \sum_{\lambda,j} \left[ M_\lambda^j - O_\lambda^j \right]^2. \quad (9)$$

Now we can perform linearization for the scaling and offset parameters that are meant to describe variable seeing conditions. Partial derivatives of  $\Phi$  over  $S^j$  and  $D^j$  can be written explicitly for each phase as they are not affected

by the radial velocities:

$$\frac{1}{2} \frac{\partial \Phi}{\partial S^j} = \sum_{\lambda} \left[ M_{\lambda}^j - O_{\lambda}^j \right] \cdot \left[ F_{\lambda \cdot (1+\gamma_j)}^* - I_{\lambda \cdot (1+\beta_j)}^j \cdot P_{\lambda \cdot (1+\delta_j)} \right] \cdot e^{-\tau_{\lambda} \cdot z_j} \quad (10)$$

$$\frac{1}{2} \frac{\partial \Phi}{\partial D^j} = \sum_{\lambda} \left[ M_{\lambda}^j - O_{\lambda}^j \right]. \quad (11)$$

For the minimum of  $\Phi$ , these derivatives should be equal to zero, which allows us to write a system of two linear equations for each pair of  $S^j$  and  $D^j$ :

$$\begin{aligned} S^j \cdot \sum_{\lambda} \left[ F_{\lambda \cdot (1+\gamma_j)}^* - I_{\lambda \cdot (1+\beta_j)}^j \cdot P_{\lambda \cdot (1+\delta_j)} \right]^2 \cdot e^{-2\tau_{\lambda} \cdot z_j} + D^j \cdot \sum_{\lambda} \left[ F_{\lambda \cdot (1+\gamma_j)}^* - I_{\lambda \cdot (1+\beta_j)}^j \cdot P_{\lambda \cdot (1+\delta_j)} \right] \cdot e^{-\tau_{\lambda} \cdot z_j} = \\ = \sum_{\lambda} O_{\lambda}^j \left[ F_{\lambda \cdot (1+\gamma_j)}^* - I_{\lambda \cdot (1+\beta_j)}^j \cdot P_{\lambda \cdot (1+\delta_j)} \right] \cdot e^{-\tau_{\lambda} \cdot z_j} \\ S^j \cdot \sum_{\lambda} \left[ F_{\lambda \cdot (1+\gamma_j)}^* - I_{\lambda \cdot (1+\beta_j)}^j \cdot P_{\lambda \cdot (1+\delta_j)} \right] \cdot e^{-\tau_{\lambda} \cdot z_j} + D^j \cdot \sum_{\lambda} 1 = \sum_{\lambda} O_{\lambda}^j. \end{aligned} \quad (12)$$

Different orbital phases are only connected in Equations 12 through the assumption of constant stellar flux, telluric absorption, and the planetary blocking function, and thus  $S$  and  $D$  can be separately evaluated for each orbital phase  $j$ .

Now we continue with the flux  $F_{\lambda}^*$ . For this, we will use the forward model in Equation 8 with our approximation for limb darkening. We shall also shift to the stellar restframe and assume unresolved stellar rotation  $\gamma_j = \beta_j$ . In practice, it means  $v \sin i \leq 1.5 \text{ km s}^{-1}$  for observations at spectral resolution of 100 000.

$$M_{\lambda \cdot (1-\gamma_j)}^j = \left[ F_{\lambda}^* - F_{\lambda}^* \cdot \frac{L_j}{N} \cdot P_{\lambda \cdot (1+\delta_j-\gamma_j)} \right] \cdot e^{-\tau_{\lambda} \cdot (1-\gamma_j) \cdot z_j} \cdot S^j + D^j \quad (13)$$

$$\Phi = \sum_{\lambda, j} \left[ M_{\lambda \cdot (1-\gamma_j)}^j - O_{\lambda \cdot (1-\gamma_j)}^j \right]^2. \quad (14)$$

Expression for the partial derivatives of  $\Phi$  over  $F_{\lambda}^*$  is given below:

$$\frac{1}{2} \frac{\partial \Phi}{\partial F_{\lambda}^*} = \sum_j \left[ M_{\lambda \cdot (1-\gamma_j)}^j - O_{\lambda \cdot (1-\gamma_j)}^j \right] \cdot e^{-\tau_{\lambda} \cdot (1-\gamma_j) \cdot z_j} \cdot S^j \cdot \left[ 1 - \frac{L_j}{N} \cdot P_{\lambda \cdot (1+\delta_j-\beta_j)} \right], \quad (15)$$

and setting it to zero allows us to obtain an expression for the stellar flux at wavelength  $\lambda$ :

$$\begin{aligned} F_{\lambda}^* \cdot \sum_j \left[ 1 - \frac{L_j}{N} \cdot P_{\lambda \cdot (1+\delta_j-\beta_j)} \right]^2 \cdot e^{-2\tau_{\lambda} \cdot (1-\gamma_j) \cdot z_j} \cdot S^j = \\ = \sum_j \left[ O_{\lambda \cdot (1-\gamma_j)}^j - D^j \right] \cdot \left[ 1 - \frac{L_j}{N} \cdot P_{\lambda \cdot (1+\delta_j-\beta_j)} \right] \cdot e^{-\tau_{\lambda} \cdot (1-\gamma_j) \cdot z_j} \cdot S^j. \end{aligned} \quad (16)$$

We obtain an explicit expression for  $F_{\lambda}^*$  in each wavelength pixel but when solving one should be mindful of the cores of strong telluric lines that may “eat” all stellar flux, resulting in degenerate equations of the type  $F_{\lambda} \cdot 0 = 0$ . We deal with this by imposing Tikhonov regularization (Tikhonov et al. 1995) on the flux vector in Equation 16.

The next step is the solution for the planet blocking function  $P$ . We shift our discrepancy function  $\Phi$  to the restframe of the planet:

$$\Phi = \sum_{\lambda, j} \left[ M_{\lambda \cdot (1-\delta_j)}^j - O_{\lambda \cdot (1-\delta_j)}^j \right]^2, \quad (17)$$

and take the derivative over  $P$ :

$$\frac{1}{2} \frac{\partial \Phi}{\partial P_{\lambda}} = - \sum_{j=j_{\text{start}}}^{j_{\text{end}}} \left[ M_{\lambda \cdot (1-\delta_j)}^j - O_{\lambda \cdot (1-\delta_j)}^j \right] \cdot I_{\lambda \cdot (1+\beta_j-\delta_j)}^j \cdot e^{-\tau_{\lambda} \cdot (1-\delta_j) \cdot z_j} \cdot S^j = 0. \quad (18)$$

Note that summation over phases ( $j$ ) is restricted to the transit phases from  $j_{\text{start}}$  to  $j_{\text{end}}$  as the blocking function  $P$  is part of our model only in these phases. The expression for  $P$  is:

$$\begin{aligned} & \sum_{j=j_{\text{start}}}^{j_{\text{end}}} \left[ F_{\lambda \cdot (1+\gamma_j - \delta_j)}^* - I_{\lambda(1+\beta_j - \delta_j)}^j \cdot P_{\lambda} \right] \cdot e^{-2\tau_{\lambda} \cdot (1-\delta_j) \cdot z_j} \cdot S^{j^2} \cdot I_{\lambda(1+\beta_j - \delta_j)}^j = \\ & = \sum_{j=j_{\text{start}}}^{j_{\text{end}}} O_{\lambda \cdot (1-\delta_j)}^j \cdot I_{\lambda(1+\beta_j - \delta_j)}^j \cdot e^{-\tau_{\lambda} \cdot (1-\delta_j) \cdot z_j} \cdot S^j \end{aligned} \quad (19)$$

and after some algebra:

$$P_{\lambda} = \frac{\sum_{j=j_{\text{start}}}^{j_{\text{end}}} \left[ F_{\lambda(1+\gamma_j - \delta_j)}^* e^{-\tau_{\lambda}(1-\delta_j)z_j} S^j - O_{\lambda(1-\delta_j)}^j \right] I_{\lambda(1+\beta_j - \delta_j)}^j \cdot e^{-\tau_{\lambda}(1-\delta_j)z_j} \cdot S^j}{\sum_{j=j_{\text{start}}}^{j_{\text{end}}} \left[ I_{\lambda \cdot (1+\beta_j - \delta_j)}^j \right]^2 \cdot e^{-2\tau_{\lambda} \cdot (1-\delta_j) \cdot z_j} \cdot S^{j^2}} \quad (20)$$

The above system of linear equations has a diagonal matrix, so we can write the explicit expression for  $P$  at each wavelength pixel. This has a danger that the denominator of Equation 20 may be zero in the cores of strongest telluric lines, similar to the case of the stellar flux. As for the stellar flux, this is again resolved by applying Tikhonov regularization to  $P$  to restrict high-frequency oscillations and degenerate equations. The addition of regularization transforms Equation 19 into a system of linear equations with a tri-diagonal matrix.

The last unknown function is the optical depth of telluric absorption  $\tau$ , which fortunately does not require a reference frame shift. The partial derivative of the discrepancy function looks like this:

$$\frac{1}{2} \frac{\partial \Phi}{\partial \tau_{\lambda}} \equiv - \sum_j \left( M_{\lambda}^j - O_{\lambda}^j \right) \cdot M_{\lambda}^j \cdot z_j = 0. \quad (21)$$

This time, we have a system of non-linear equations because of the  $M^2$  term. We denote the partial derivative of  $\Phi$  with  $Y$  and use the Newton-Raphson (NR) algorithm to find the solution:

$$Y \equiv \sum_j \left( M_{\lambda}^j - O_{\lambda}^j \right) \cdot M_{\lambda}^j \cdot z_j = 0. \quad (22)$$

We are looking for a set of  $\tau_{\lambda}$  that will turn  $Y$  to zero for every wavelength. To find these, we need partial derivatives of  $Y$  over  $\tau_{\lambda}$ :

$$\frac{\partial Y}{\partial \tau_{\lambda}} = - \sum_j \left( 2M_{\lambda}^j - O_{\lambda}^j \right) \cdot M_{\lambda}^j \cdot z_j^2. \quad (23)$$

The NR expressions for  $\tau_{\lambda}$  corrections is given by the first order Taylor expansion:

$$\Delta \tau_{\lambda} = \frac{\sum_j \left( M_{\lambda}^j - O_{\lambda}^j \right) \cdot M_{\lambda}^j \cdot z_j}{\sum_j \left( 2M_{\lambda}^j - O_{\lambda}^j \right) \cdot M_{\lambda}^j \cdot z_j^2}. \quad (24)$$

We hope that our model is close enough to the observations so that the difference in the denominator never turns to zero. At this point, we started thinking about finding a good initial guess as NR convergence depends on it. Numerical experiments showed that any form of the initial guess for  $e^{-\tau_{\lambda}}$  that is in between 1 and the continuum normalized observation at a minimum airmass is good enough for a stable solution. The NR solver is iterative and stops when the maximum correction for  $\tau$  is less than the adopted threshold, and convergence is typically achieved faster for segments with stronger tellurics.

#### 2.4. Solving the equations

Let us write the final set of equations in a single place.

Forward model :

$$N = \pi \cdot \left( 1 - \sum_{k=1}^4 \frac{k \cdot a_k}{k+4} \right) \quad (25)$$

$$L_j = 1 - \sum_{k=1}^4 a_k \cdot (1 - \mu_j^{k/2}) \quad (26)$$

$$M_\lambda^j = \left[ F_{\lambda \cdot (1+\gamma_j)}^* - F_{\lambda \cdot (1+\beta_j)}^* \cdot \frac{L_j}{N} \cdot P_{\lambda \cdot (1+\delta_j)}^j \right] \cdot e^{-\tau_\lambda \cdot z_j} \cdot S^j \quad (27)$$

Stellar flux :

$$F_\lambda^* = \frac{\sum_j O_{\lambda \cdot (1-\gamma_j)}^j \cdot \left[ 1 - \frac{L_j}{N} \cdot P_{\lambda \cdot (1+\delta_j-\gamma_j)} \right] \cdot e^{-\tau_\lambda \cdot (1-\gamma_j) \cdot z_j} \cdot S^j}{\sum_j \left[ 1 - \frac{L_j}{N} \cdot P_{\lambda \cdot (1+\delta_j-\gamma_j)} \right]^2 \cdot e^{-2\tau_\lambda \cdot (1-\gamma_j) \cdot z_j} \cdot S^{j^2}} \quad (28)$$

Slit losses and background :

$$\begin{aligned} & S^j \cdot \sum_\lambda \left[ F_{\lambda \cdot (1+\gamma_j)}^* - F_{\lambda \cdot (1+\beta_j)}^* \cdot \frac{L_j}{N} \cdot P_{\lambda \cdot (1+\delta_j)} \right]^2 \cdot e^{-2\tau_\lambda \cdot z_j} + \\ & + D^j \cdot \sum_\lambda \left[ F_{\lambda \cdot (1+\gamma_j)}^* - F_{\lambda \cdot (1+\beta_j)}^* \cdot \frac{L_j}{N} \cdot P_{\lambda \cdot (1+\delta_j)} \right] \cdot e^{-\tau_\lambda \cdot z_j} = \end{aligned} \quad (29)$$

$$\begin{aligned} & = \sum_\lambda O_\lambda^j \left[ F_{\lambda \cdot (1+\gamma_j)}^* - F_{\lambda \cdot (1+\beta_j)}^* \cdot \frac{L_j}{N} \cdot P_{\lambda \cdot (1+\delta_j)} \right] \cdot e^{-\tau_\lambda \cdot z_j} \\ & S^j \cdot \sum_\lambda \left[ F_{\lambda \cdot (1+\gamma_j)}^* - F_{\lambda \cdot (1+\beta_j)}^* \cdot \frac{L_j}{N} \cdot P_{\lambda \cdot (1+\delta_j)} \right] \cdot e^{-\tau_\lambda \cdot z_j} + D^j \cdot \sum_\lambda 1 = \sum_\lambda O_\lambda^j \end{aligned} \quad (30)$$

Telluric optical depth :

$$\Delta\tau_\lambda = - \frac{\sum_j \left[ M_\lambda^j - O_\lambda^j \right] \cdot M_\lambda^j \cdot z_j}{\sum_j \left( 2M_\lambda^j - O_\lambda^j \right) \cdot M_\lambda^j \cdot z_j^2} \quad (31)$$

Planet blocking function :

$$P_\lambda = \frac{\sum_j \left[ F_{\lambda(1+\gamma_j-\delta_j)}^* e^{-\tau_\lambda(1-\delta_j)z_j} S^j - O_{\lambda(1-\delta_j)}^j \right] F_{\lambda(1+\beta_j-\delta_j)}^* \cdot \frac{L_j}{N} \cdot e^{-\tau_\lambda(1-\delta_j)z_j} \cdot S^j}{\sum_j \left[ F_{\lambda \cdot (1+\beta_j-\delta_j)}^* \cdot L_j / N \right]^2 \cdot e^{-2\tau_\lambda \cdot (1-\delta_j) \cdot z_j} \cdot S^{j^2}} \quad (32)$$

The unknowns are the optical thickness of telluric absorption  $\tau_\lambda$ , the stellar flux  $F_\lambda^*$ , the planetary blocking function  $P_\lambda$ , and the scaling and offset parameters of observations  $S^j$  and  $D^j$ .

We have no hope of solving the whole system of equations simultaneously, so we set up an iterative scheme starting with computing stellar flux (Equations 25–28), updating scaling/offset (Equations 29–30), then correcting telluric optical depths (Equation 31), and, finally, deriving the planet blocking function (Equation 32). We use regularization in the wavelength dimension for  $F_\lambda^*$ ,  $\tau_\lambda$ , and  $P_\lambda$  to avoid possible division by zero and high-frequency noise. The procedure then repeats until the maximum relative change of the unknown functions is less than some reasonable value, e.g.  $10^{-4}$ .

There is some degeneracy between unknown vectors, even though they appear orthogonal in the data space (wavelength versus time or phase). For example, one can multiply the value of the scaling vector  $S$  and divide the stellar flux  $F_\lambda^*$  by the same amount. This degeneracy is removed by fixing the value of  $S$  at one particular phase (e.g. setting  $S_j$  to 1 at the phase with the highest measured flux).

## 2.5. Implementation

The algorithm described in the previous section was implemented using the IDL programming language, with a Python port being currently in development. The IDL code consists of the data input part, the initialization (initial guesses for all unknown functions) and the main loop that updates one unknown function at a time. The main loop calls sequentially four solvers (for stellar flux, scaling/offset, telluric optical depth, and planet blocking function) and it ends

when the maximum number of iterations or convergence is achieved. The input data consists of observations grouped in individual transits, spectral intervals (e.g. from echelle orders or detectors) and orbital phases. As previously stated, we assume constant stellar flux and planet blocking function between transits but telluric absorption and observing conditions can change.

Observations are complemented by planetary and barycentric RVs used to compute the Doppler factors  $\gamma$ ,  $\beta$ , and  $\delta$  as well as the planet shadow location with respect to the stellar center (for computing blocked fraction of the stellar flux). Throughout the computation, the observations and other functions of wavelength need to be interpolated onto a different wavelength grid due to Doppler shifts. This is done using cubic splines and we avoid extrapolation. Only the parts of relevant vectors that can be evaluated without extrapolation are used by the solvers. As the result, the ends of spectral intervals are less constrained by the observations and rely more on regularization. The fact that we process one unknown function at a time slows somewhat the conversion: a typical run takes 600–1000 iterations, corresponding to  $\sim 0.5$  hour on a modern desktop computer (Apple M2 Ultra CPU) using 114 phases and 6000 wavelength points.

The implementation of the TSD algorithm described above was tested using simulated data. To achieve this, we have developed a sophisticated simulation tool, capable of generating high-resolution “observed” spectra given the stellar flux spectrum, stellar specific intensities, the telluric absorption and the planetary transmission spectrum. The transit-specific parameters and instrument signatures can be replicated using real transits of real exoplanets and existing instruments. The output of the simulator has the same structure as the real data preparation tool: a single FITS file containing all the necessary information for the TSD code. The specifics of this simulator are described in the next section.

### 3. TSD PERFORMANCE ON SIMULATED DATA

Alongside the development of the TSD we developed software<sup>9</sup> to produce simulated exoplanet transmission spectroscopy observations. The combination of having a known ground ‘truth’ for such simulations and the ability to generate simulations with several transits and arbitrary S/N values—something not shared by real data—was essential for testing and benchmarking TSD during its development. For comparison purposes, we first simulated two real transits observed by VLT/CRIRES+ (i.e. matching the exposure midpoints and durations, airmasses, and barycentric velocities of the real data) and an additional five real, but unobserved, transits. In order to run, the simulator requires template stellar, telluric, and exoplanet spectra; an adopted instrumental setup including spectral resolution and wavelength scale; data uncertainties, an exoplanet orbital solution and associated velocities. Subsection 3.1 describes our test case exoplanet system WASP-107 b, adopted system parameters, and model stellar and exoplanet spectra; Subsection 3.1.3 describes our adopted model telluric spectra; Subsection 3.2 describes the simulation methodology itself; and finally, Subsection 3.3 shows results and performance of the new algorithm when tested on simulated transmission spectroscopic data.

#### 3.1. The WASP-107 b System

WASP-107 b is a warm super-Neptune orbiting a late K dwarf of spectral type K6, originally discovered by the WASP (Wide Angle Search for Planets, [Pollacco et al. 2006](#)) ground-based exoplanet transit survey in 2017 ([Anderson et al. 2017](#)). Despite only having a mass of  $0.12 M_{\text{Jup}}$ , it has a remarkably low density with a radius nearly that of Jupiter at  $0.94 R_{\text{Jup}}$ , resulting in a transit depth of 2.17%. This, plus its short orbital period of 5.7 days, makes it highly amenable to atmospheric characterization at both low and high spectral resolution. It is known to have an extended helium-rich atmosphere and comet-like helium tail ([Spake et al. 2018](#); [Allart et al. 2019](#); [Kirk et al. 2020](#); [Spake et al. 2021](#); [Guilluy et al. 2024](#)). Previous studies detected a number of key molecular species including  $\text{H}_2\text{O}$ ,  $\text{CH}_4$ ,  $\text{CO}$ ,  $\text{CO}_2$ ,  $\text{SO}_2$ , and  $\text{NH}_3$  ([Kreidberg et al. 2018](#); [Dyrek et al. 2024](#); [Welbanks et al. 2024](#)).

The planet follows a misaligned and nearly polar orbit, with [Rubenzahl et al. \(2021\)](#) demonstrating the retrograde motion of the planet using the Rossiter-McLaughlin (RM, [Rossiter 1924](#); [McLaughlin 1924](#)) effect measured with the Keck HIRES spectrometer. Importantly, the RM effect provides a direct measurement (rather than an upper limit) of the stellar  $v \sin i$  by observing the fraction of the projected stellar rotational velocity that is blocked by the transiting planet. [Rubenzahl et al. \(2021\)](#) derived the value of  $v \sin i$  of  $0.45 \text{ km s}^{-1}$  compatible with the approximation for the limb darkening that we introduced in Section 2.2. The low stellar  $v \sin i$  and high planet obliquity is advantageous for

<sup>9</sup> Python code for interfacing with data reduction software, handling of template spectra, our exoplanet transmission spectroscopy simulator, and observational data cleaning and preparation can be found at <https://github.com/adraings/luciferase>.

**Table 1.** WASP-107 system stellar, planet and orbital parameters.

Parameter	Unit	Value	Reference
Star			
Gaia DR3 ID	-	3578638842054261248	Vallenari et al. (2023)
2MASS ID	-	2MASS J12333284-1008461	Skrutskie et al. (2006)
RA	hh:mm:ss.ss	12 33 32.74	Vallenari et al. (2023)
Dec	dd:mm:ss.ss	-11 51 13.62	Vallenari et al. (2023)
Parallax	mas	$15.5277 \pm 0.0260$	Vallenari et al. (2023)
Distance	pc	$64.40 \pm 0.03$	Vallenari et al. (2023)
RV	$\text{km s}^{-1}$	$14.06 \pm 0.20$	Vallenari et al. (2023)
$K_S$ mag	-	$8.637 \pm 0.023$	Skrutskie et al. (2006)
$M_\star$	$M_\odot$	$0.683 \pm 0.017$	Piaulet et al. (2021)
$R_\star$	$R_\odot$	$0.67 \pm 0.02$	Piaulet et al. (2021)
$T_{\text{eff}}$	K	$4425 \pm 70$	Piaulet et al. (2021)
$v \sin i$	$\text{km s}^{-1}$	$2.5 \pm 0.8$	Anderson et al. (2017)
Planet			
$M_P$	$M_\oplus$	$30.5 \pm 1.7$	Piaulet et al. (2021)
$R_P$	$R_\oplus$	$10.04 \pm 0.2$	Močnik et al. (2017)
$a$	AU	$0.0553 \pm 0.0013$	Močnik et al. (2017)
$e$	-	$0.06 \pm 0.04$	Piaulet et al. (2021)
$i$	deg	$89.56 \pm 0.078$	Močnik et al. (2017)
$K$	$\text{m s}^{-1}$	$14.1 \pm 0.8$	Skrutskie et al. (2006)
Transit Duration	hr	$2.73864 \pm 0.00194$	Močnik et al. (2017)
JD (mid)	day	$2457584.329746 \pm 0.000011$	Močnik et al. (2017)
$P$	day	5.7214742	Piaulet et al. (2021)

transmission spectroscopy observations at high spectral resolution, with both serving to lower the significance of the RM signature on our observations and simulations.

Its puffy atmosphere, favorable orbital geometry, and confirmed atmospheric detections, plus the slow rotation of its stellar host, make it an excellent test system for atmospheric characterization and thus for demonstrating TSD. However, in practice, characterization of WASP-107 b at high spectral resolution in the infrared is a relatively unexplored regime. A recent study by Boldt-Christmas et al. (2025) analyzed the very same WASP-107 b VLT/CRIRES+ observations used in this paper (see Section 4), and that study demonstrated that (i) this target is clearly challenging to study in the  $K$  band at high resolution from the ground using more traditional analysis techniques of SYSREM and cross-correlation, largely thanks to tellurics and the target’s high altitude cloud deck quenching spectral features; (ii) these challenges are expected to be in play for many other similarly cooler, cloudy targets (i.e. not hot Jupiters) and should thus be addressed by evolving methodology in the field. This result is one of many that underline some of the limitations of common detrending methods (see discussion in Section 1), especially for cooler exoplanet targets, which is one of the major motivations for this work.

Sections 3.1.1 and 3.1.2 describe synthetic stellar and planet transmission spectra used in our simulations. The adopted stellar and planetary parameters are listed in Table 1, and we have confirmed stellar parameters using the SME tool (Piskunov & Valenti 2017) and ESO HARPS observations of WASP-107 from 2018 (program 0100.C-0750(D)).

### 3.1.1. WASP-107 Stellar Spectrum

We computed the stellar spectrum using a 1D LTE<sup>10</sup> spherically symmetric MARCS model atmosphere (Gustafsson et al. 2008) and the associated BSYN radiative transfer software at  $R \sim 200\,000$  for  $T_{\text{eff}} = 4420\text{ K}$ ,  $\log g = 4.61$ ,  $[\text{M}/\text{H}] = 0.05$ . This version of MARCS adopts solar abundances by Grevesse et al. (2007),  $[\alpha/\text{Fe}]$  scaled by the metallicity  $[\text{Fe}/\text{H}]$ , line data per the VALD-2 database (Stempels et al. 2001), and opacity tables per references in Gustafsson

<sup>10</sup> Local Thermodynamic Equilibrium

et al. (2008). The use of the spherically symmetric model atmosphere enables more accurate computation of specific intensity spectra at the starting and ending phases of the transit. For this work, we sample 49 different  $\mu$  angles across the disk of the star with density increasing toward the limb, and with uniform sampling in wavelength. This is sufficient to perform interpolation of specific intensities to the position of the planet throughout the transit, *without* involving any approximation for limb-darkening approximation.

### 3.1.2. WASP-107 b Transmission Spectrum

We generated the template exoplanet spectra using the Python radiative transfer package `petitRADTRANS` version 2.7.6<sup>11</sup> (Mollière et al. 2019). We included absorption from H<sub>2</sub>O (Polyansky et al. 2018), CO (Rothman et al. 2010), NH<sub>3</sub> (Yurchenko et al. 2011) based on the analysis of WASP-107 b in Boldt-Christmas et al. (2025). The templates were initially generated at a spectral resolution of  $R = 10^6$  over the 1.6–3.0  $\mu\text{m}$  wavelength range, and later convolved and clipped to match the nominal resolving power ( $R = 100,000$ ) and wavelength range (2.0–2.5  $\mu\text{m}$ ) of the real CRRES+  $K$  band observations. The assumed parameters for the planetary atmosphere came primarily from the recent JWST studies of WASP-107 b such as Dyrek et al. (2024), Welbanks et al. (2024), and Sing et al. (2024) including  $T_{\text{int}} = 460$  K,  $T_{\text{eq}} = 738$  K, and  $R_p = 0.94 R_J$ . A complete list of input parameters in simulating the exoplanet transmission spectrum can be found in Table 3 of Boldt-Christmas et al. (2025).

### 3.1.3. Molecfit Telluric Model

To generate a template telluric spectrum for our simulations, we make use of the `Molecfit` software package (Smette et al. 2015; Kausch et al. 2015), which was developed as a model-based alternative to the traditional—but observationally expensive—approach of observing telluric reference stars interleaved with science targets over a night. `Molecfit` is designed to remove telluric features from science observations, and it does this by computing an initial guess taking into account the real atmospheric profile at the telescope location at the time of the science observations and morphs it to find the best match to predicted telluric features by adjusting abundances, broadening, and additional parameters. The synthetic telluric spectrum is computed by solving radiative transfer line-by-line using a large collection of data for all molecular absorbers present in the Earth atmosphere (including H<sub>2</sub>O, CO, CO<sub>2</sub>, CH<sub>4</sub>—the main species affecting the  $K$  band).

We require one unique telluric transmission spectrum per simulated night. To that end, we use `Molecfit` to fit seven real VLT/CRRES+ observations in the K2148 setting: two actually of WASP-107 b, and in lieu of additional WASP-107 b observations, another five transits of GJ 1214 b, all observed as part of Guaranteed Time Observations (GTO) for CRRES+. To improve the fit, these observations were pre-processed as described in Section 4.1 in order to reduce the reliance on `Molecfit`’s own continuum correction capability. Starting with blaze-correction of CRRES+ spectra, continuum normalization was done separately for each spectral order and each of the three detectors using a linear polynomial fit. The ‘continuum’ points were selected by eye and strong stellar lines identified by comparison against the synthetic stellar spectrum were masked out as explained in Section 3.1.1. `Molecfit` was used in a two-step iterative process to improve the final telluric fit. After the first `Molecfit` iteration, we tune the continuum polynomial with respect to the CRRES+ observations, synthetic stellar spectrum, and the initial telluric model. Then we run `Molecfit` a second time to produce the final adopted telluric model for the night in question.

## 3.2. Simulation Methodology

Our exoplanet transmission spectroscopy simulations consist of two main steps. The first involves the compilation of the so-called ‘time-step info’ for each exoplanet phase (i.e. observed spectrum) for each night to be modeled. This includes compiling self-consistent timing, positional, and velocity information from the real observations (including number of exposures, exposure times, airmasses, barycentric velocities), as well as computing orbital geometry of the exoplanet itself (e.g. projected planet positions and velocities, orbital phase). The second step involves the simulator proceeding nightly to model each phase via Equation 1 using our template stellar, telluric, and exoplanet spectra, plus the per-phase time-step information. Critically, we model the *extracted* 1D spectra for each phase, and do not simulate individual optical elements, detectors, telescope nodding, or data-reduction—instead approximating these as a series of transfer functions. We compute and interpolate each component of the equation separately—disk integrated flux (RV frame  $\gamma$ ), exoplanet transmission spectrum (RV frame  $\beta$ ), planet ‘shadow’ (RV frame  $\delta$ ), airmass-scaled telluric

<sup>11</sup> <https://petitradtrans.readthedocs.io/>

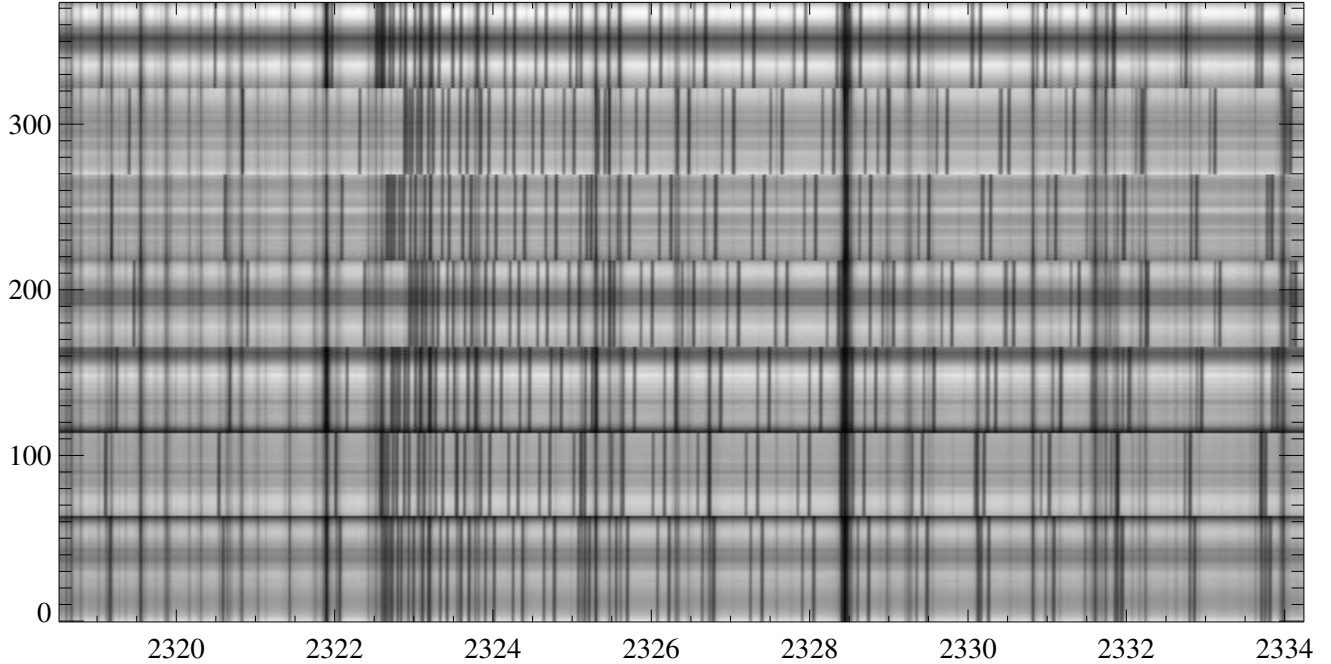


**Figure 2.** A wavelength fragment of the simulated seven-transit observations of WASP-107 b with VLT/CRIRES+. The wavelength range (horizontal axis, nm) corresponds to the part of spectral order 24 (second order from the bottom) that falls on the middle detector, and the vertical axis is the time dimension starting with exposure 0 of the first observation at the bottom. Horizontal bands correspond to individual transits with 50-64 spectra per transit, with the influence of airmass and variable slit losses affecting the flux level between adjacent exposures. One can clearly distinguish telluric (constant in wavelength) and stellar (shifting with barycentric velocity) lines and notice the variation of telluric absorption strength between transits.

transmission, and scaling value representing the slit losses.<sup>12</sup> Finally, the spectra are convolved with the instrumental transfer function, and a realistic noise pattern is added. The S/N of 130 and slit losses were estimated using the real observations of WASP-107 b with CRIRES+ analyzed in Boldt-Christmas et al. (2025) and in Section 4. The interpolation to the detector pixels is performed with cubic spline using the `interp1d` function of Python’s `scipy`.

The result is one datacube of fluxes and uncertainties per transit of shape  $[N_{\text{phase}}, N_{\text{spec}}, N_{\text{px}}]$ , alongside a table of time-step information of length  $N_{\text{phase}}$ , where  $N_{\text{phase}}$  is the number of phases, modelled for this night;  $N_{\text{spec}}$  is the number of spectral segments (three detectors per spectral order for CRIRES+); and  $N_{\text{px}}$  is the number of spectral pixels per spectral segment. The spectra and time-step information for all nights simulated are then packaged in the same custom FITS file format as the real data, allowing TSD to be agnostic as to whether it is running on real or simulated data.

### 3.3. Model Performance

For testing the performance of the TSD we have produced simulated data for seven transits of WASP-107 b as described in Section 3.1, with a representative spectral order shown in Figure 2. This illustrates the main reason TSD works: different transits separate or ‘shuffle’ the stellar and telluric features because of the change of the barycentric velocity from night-to-night, while the orbital motion of the planet allows one to distinguish the planet transmission from the other two components. The latter, of course, requires high spectral resolution only possible from the ground.

The TSD inversion procedure was run on the first two, three, four, five, six, and then all seven simulated transits to test how the number of transits influences the quality of the recovery. Convergence was typically achieved after about 800 iterations based on the maximum change in the effective blocking area of the planet  $P$ . Figure 3 shows the reconstruction when running on all seven simulated nights of (i) the telluric spectrum (night #2 of 7) on the top, and

<sup>12</sup> Note that we do not simulate the offset term  $D^j$  from Equation 1. The extra background offset was a provision to account for imperfect nodding pair subtraction. When applied to the real data it turned out to be insignificant (less than 5 photoelectrons).

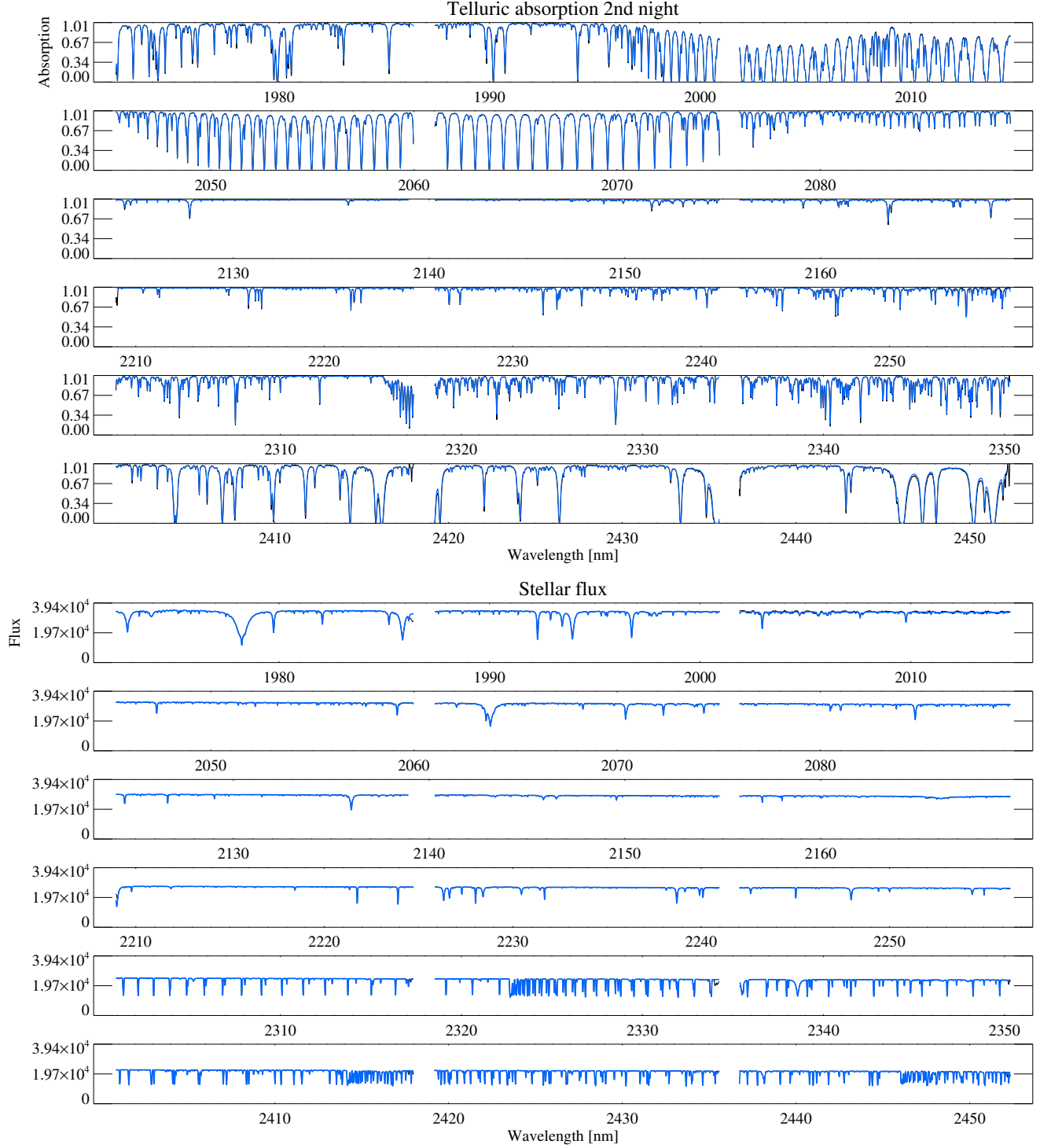


**Figure 3. Top:** Reconstruction of the telluric absorption from the simulated seven transit observations of WASP-107 b (in black) for the second transit. 6 spectral orders registered by CRIRES+ in K band are shown vertically with 3 horizontal segments corresponding to CRIRES+ detectors. The true solution used in the simulations (without noise) is shown in blue. Note that TSD solves for optical thickness  $\tau$  and what is plotted is the telluric absorption in zenith  $e^{-\tau}$ . **Bottom:** As above, but for the reconstruction of the stellar flux.

(ii) the stellar flux on the bottom. Note that we choose to show telluric *absorption* even though TSD works with the optical thickness because it is easier to see the interdependence between tellurics and other unknown functions in this

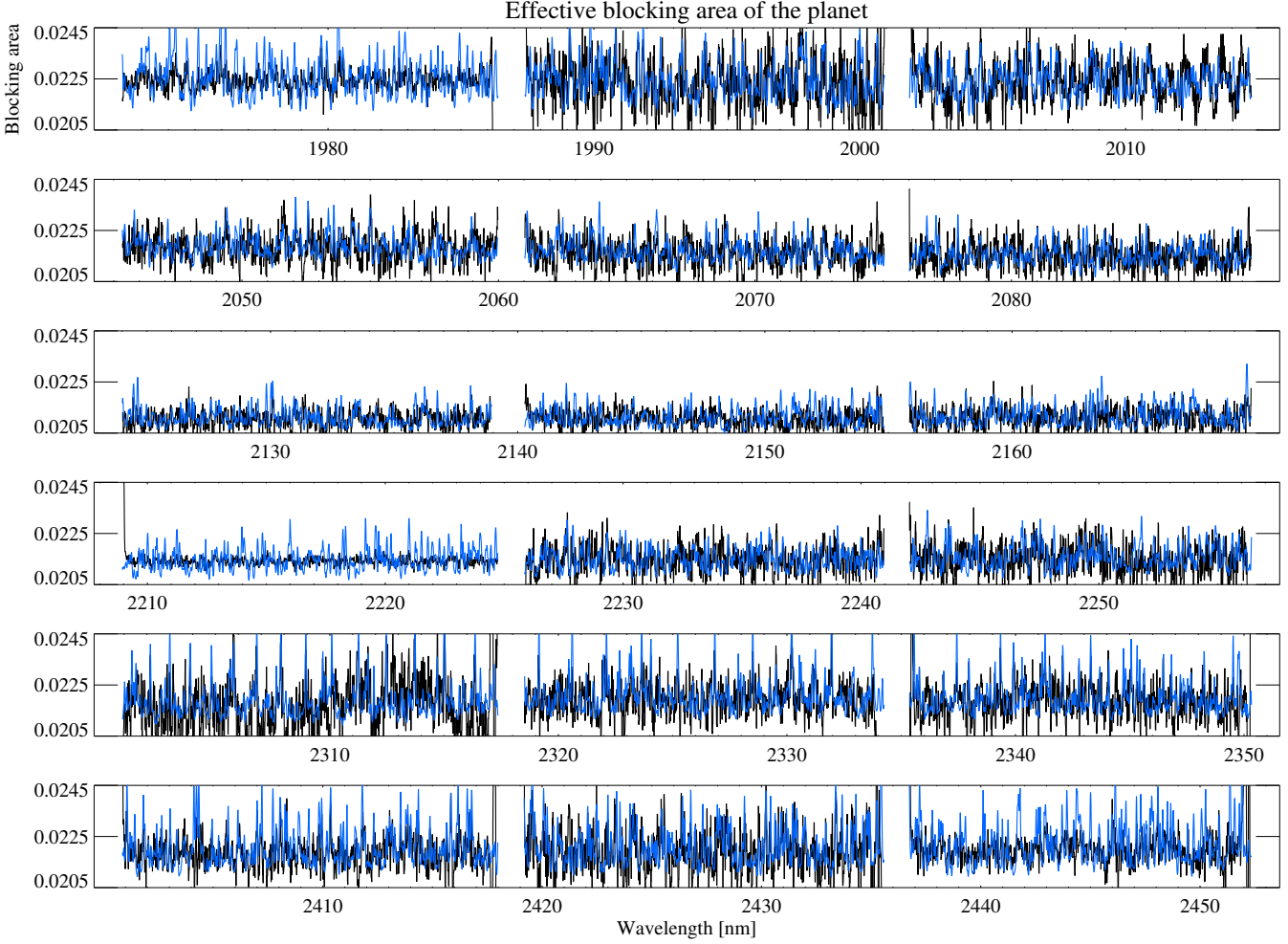


**Figure 4.** As Figure 3, but for the planetary component of WASP-107 b. The black line is the reconstruction of the planet effective blocking area based on seven simulated transits of WASP-107 b, and the true—and zero noise—solution that went into simulations is shown in blue. A zoom in view of the recovery for detector 2 is shown in Figure 5.

way. The reconstruction (in black) is barely visible behind the input telluric absorption (in blue) and while occasional discrepancies are found in the end of spectral segments, this is to be expected when avoiding extrapolation as we do. Generally, the reconstruction of tellurics and stellar flux is close to perfect considering that the S/N of an individual spectrum (i.e. a single phase) is around 130.

Finally, the transmission spectrum of the planet (the effective blocking area of the planet  $P$  to be precise) based on seven transits is shown in Figure 4. The quality is obviously inferior to the other unknown function, but we have to remember that here the signal is at the level of a few 0.1 % of the stellar flux. This figure allows us to draw two main conclusions: (1) the mean level of the recovered transmission spectrum (2.2 %) matches that of the template and (2) most of transmission variations are well reproduced. Major discrepancies, such as at 1978, 1986, 1994, and 1994 nm, are associated with strong and broad stellar features. The RV excursion of the transmission spectrum during transits does not exceed the width of these features (a few tens of  $\text{km s}^{-1}$ ) and so the reconstruction fails. This is clearly a limitation of our method. One can also notice the “edge effects” in several wavelength segments (e.g. on the right side of each segment in the two bottom orders). This is again related to the algorithm avoiding extrapolation of unknown vectors, and so not all phases contribute to these wavelengths when linearization matrices are computed.

To examine recovery at the limit of our spectral resolution ( $3 \text{ km s}^{-1}$ ), we zoom in on the central detector in Figure 5. The reconstruction looks good, but how good is it actually? Table 2 presents the Root Mean Square (RMS) for each spectral interval, as well as the values of the peaks of cross-correlation between the input transmission (effective blocking function) and its reconstruction. Note that only the top two numbers in each cell of this table refer to the simulations,

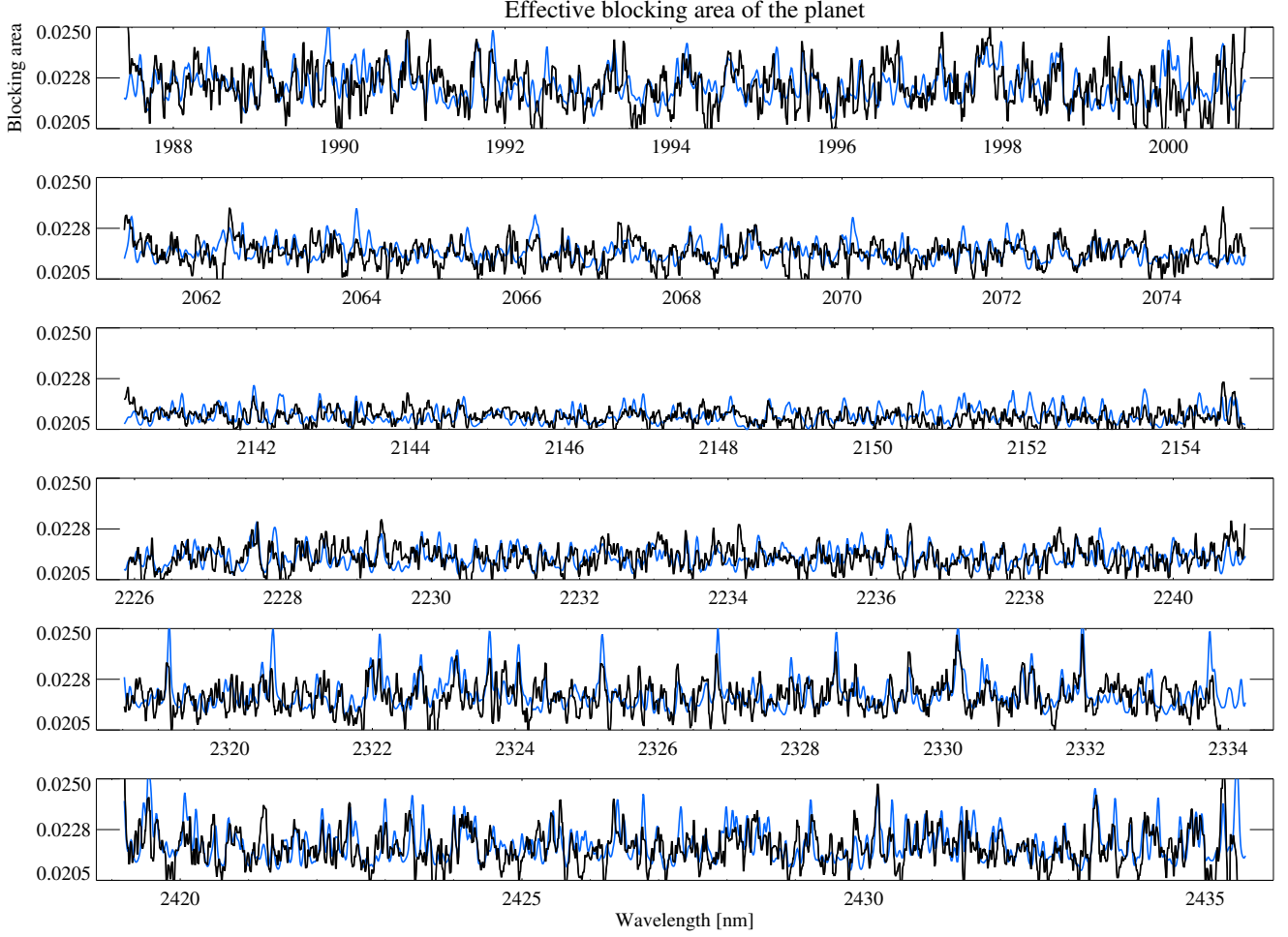
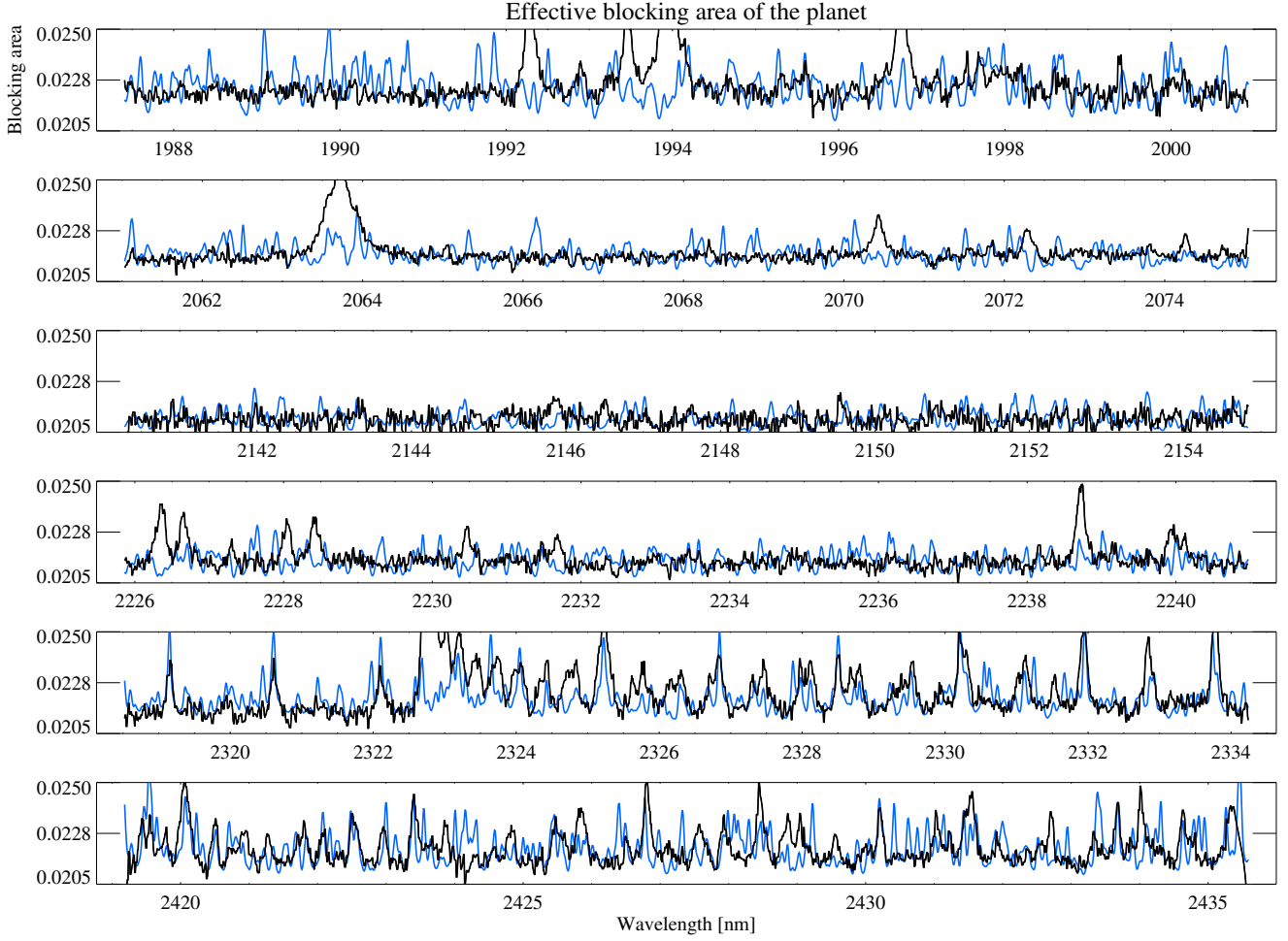


**Figure 5.** Zoom-in on the central detector (detector 2) in Figure 4. Reconstruction is again shown in black, and the true solution is in blue. Note that while the reconstruction is far from 1:1, the reconstruction does consistently recover the average blocking radii of the planet and certain strong spectral features like those of CO lines in the two reddest orders.

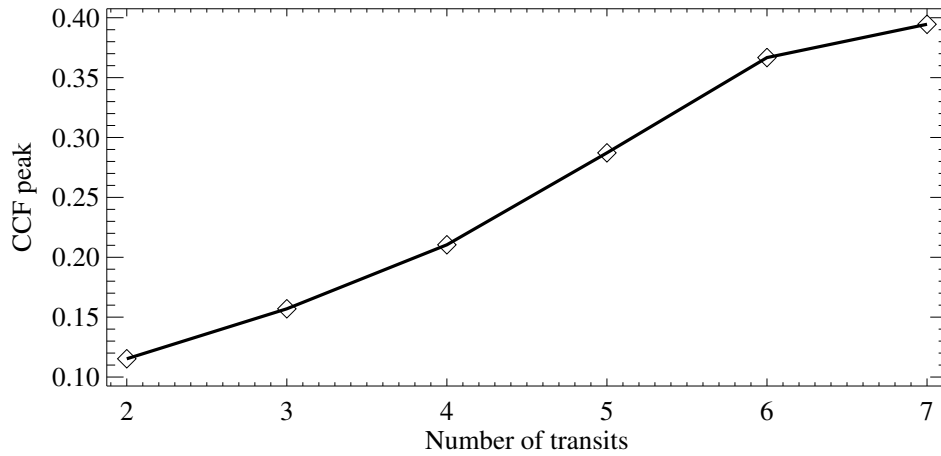
as the third number refers to the real data analyzed in Section 4. The values in the table change significantly between spectral segments affected by the strength and number of spectral features present in each segment, but they give a good sense of improvement when increasing the number of transits.

Figure 6 shows the reconstruction based on only the two simulated transits that correspond to our actual data set for WASP-107 b. We clearly see that artifacts associated with the broad stellar lines are heavily amplified, and that reconstruction of the top two orders, dominated by water absorption, essentially failed. The failure is quantified by the peak of the cross-correlation function (CCF) for this order presented in Table 6 (0.0178 for two nights versus 0.2985 for seven in case of the middle detector). This is not surprising considering the density and strength of water lines in the telluric spectrum and difficulty distinguishing between the stellar and telluric spectra using just two transits. The two bottom spectral orders containing CO lines are successfully recovered in both simulations thanks to lower strength of CO lines in the stellar spectrum and fewer, more well-separated telluric lines.

An abundance of small-scale features can be seen in the seven-transit reconstruction (black line in Figure 5) compared to the two-night test. The inversion code uses the Tikhonov regularization (as mentioned in Section 2.3) for unknown functions to prevent nonphysical values (e.g. negative values of the blocking function). The impact of regularization is most significant for the transmission spectrum, where it controls the trade-off between the S/N and spectral resolution of the result. The relative weight of the contribution of regularization is higher for the two-transit case, as there are fewer observational data.



**Figure 6.** The same as in Figure 5 but based on the two first transits only. Note that regularization damps the small-scale features seen in the seven-night reconstruction, but it cannot remove large artifacts appearing due to the difficulty of disentangling spectral components given only two nights of data.



**Figure 7.** Maximum of the cross-correlation function (CCF) between the true and the recovered transmission spectrum (effective blocking area) of the planet as a function of the number of transits given to the TSD (averaged for all spectral intervals). Note that the CCF peak increases along with the number of transits, indicating how additional transits with different or ‘shuffled’ barycentric velocities help to improve S/N and reduce degeneracies during the inversion procedure.

**Table 2.** Numerical assessment of the reconstruction results for simulations with two and seven transits as well as for the two-transit real data of WASP-107 b. The format of the table is similar to the layout of Figures 3 and 4. The rows corresponds to spectral order numbers and columns - to detectors. Each cell contains a stack of three numbers: RMS or cross-correlation peak for simulated two (top), seven (in bold) or real data (italic). Note that a direct comparison between simulated and real data is not possible as the true spectrum of WASP-107 b is not known to us.

Order	Det 1		Det 2		Det 3	
	RMS	CC	RMS	CC	RMS	CC
28	0.00102	0.0498	0.00102	0.0178	0.00072	0.1775
	<b>0.00096</b>	<b>0.1551</b>	<b>0.00085</b>	<b>0.2985</b>	<b>0.00073</b>	<b>0.1935</b>
	<i>0.00136</i>	<i>0.0841</i>	<i>0.02404</i>	<i>0.0190</i>	<i>0.00112</i>	<i>0.0701</i>
27	0.00061	0.0522	0.00054	0.1858	0.00051	0.1157
	<b>0.00051</b>	<b>0.3264</b>	<b>0.00049</b>	<b>0.3043</b>	<b>0.00046</b>	<b>0.2871</b>
	<i>0.00074</i>	<i>0.0414</i>	<i>0.01549</i>	<i>0.0860</i>	<i>0.00069</i>	<i>0.0782</i>
26	0.00047	0.0941	0.00046	0.1203	0.00050	0.1957
	<b>0.00043</b>	<b>0.2496</b>	<b>0.00044</b>	<b>0.2106</b>	<b>0.00048</b>	<b>0.2519</b>
	<i>0.00050</i>	<i>0.0205</i>	<i>0.02681</i>	<i>0.1075</i>	<i>0.00060</i>	<i>0.1725</i>
25	0.00059	0.0159	0.00057	0.0163	0.00066	0.0186
	<b>0.00061</b>	<b>0.0610</b>	<b>0.00051</b>	<b>0.2103</b>	<b>0.00056</b>	<b>0.2964</b>
	<i>0.00068</i>	<i>0.0502</i>	<i>0.03960</i>	<i>0.1395</i>	<i>0.00082</i>	<i>0.1335</i>
24	0.00078	0.4100	0.00084	0.2816	0.00079	0.2395
	<b>0.00063</b>	<b>0.6047</b>	<b>0.00070</b>	<b>0.4760</b>	<b>0.00075</b>	<b>0.2780</b>
	<i>0.00141</i>	<i>0.1958</i>	<i>0.05115</i>	<i>0.1746</i>	<i>0.00124</i>	<i>0.1795</i>
23	0.00090	0.2747	0.00089	0.3165	0.00099	0.2324
	<b>0.00085</b>	<b>0.3284</b>	<b>0.00089</b>	<b>0.3519</b>	<b>0.00098</b>	<b>0.2403</b>
	<i>0.00128</i>	<i>0.2393</i>	<i>0.07188</i>	<i>0.2578</i>	<i>0.00112</i>	<i>0.1956</i>

Figure 7 shows how the quality of the transmission spectrum reconstruction improves with the number of transits, with the quality of the solution estimated through the cross-correlation between the TSD solution and the input transmission. This curve will have a different shape if we construct it using separate orders. For example, it will start higher for the two bottom orders in Figure 5 dominated by CO, while for the two top orders dominated by water, the rise will not start until the fifth transit is added. We also see that the addition of the seventh transit results in a minor improvement of the solution, giving some hints for potential observing strategies.

#### 4. TSD PERFORMANCE ON OBSERVED DATA

The previous section presented numeric experiments that demonstrate the ability of an inverse model like TSD to recover high-resolution transmission spectra from realistic quality data *without* model-based assumptions. In this section, we present an example of TSD’s performance on two *real* transits of WASP-107 b as observed with CRIRES+. Note that since this paper is intended primarily to present the method itself, we limit the presentation and interpretation of astrophysical results for follow-up studies.

##### 4.1. Observations and Data Reduction

CRIRES—the CRyogenic InfraRed Echelle Spectrograph—is an Adaptive Optics (AO) fed (Paufigue et al. 2004), high-resolution ( $R \sim 100\,000$  when using a  $0.2''$  slit), long-slit echelle spectrograph operating in the *YJHKLM* ( $0.92 - 5.3\,\mu\text{m}$ ) bands on ESO’s Very Large Telescope (VLT) at Cerro Paranal, Chile. The original version of the instrument was in operation between 2006 (Kaeufl et al. 2004) and 2014. After decommissioning CRIRES underwent a substantial upgrade before returning to service in 2021, gaining cross-dispersion optics, state-of-the-art detectors, a new version of the MACAO AO, and a + to its name denoting its new identity as CRIRES+ (Dorn et al. 2023). Although CRIRES always inhabited a relatively unique instrumental parameter space, a 10-fold increase in the simultaneous wavelength coverage, better throughput, and better reduction pipeline has made CRIRES+ a much more efficient and competitive instrument.

**Table 3.** Summary of VLT/CRIRES+ observations for WASP-107 b.

Parameter	Unit	Night 1	Night 2
Date (UTC)	-	2022-03-11	2023-02-23
Time (UTC)	-	03:54–09:30	04:55–09:16
$N_{\text{exp}}$ (in/out)	-	64 (34/30)	50 (34/16)
$t_{\text{exp}}$	sec	300	300
Airmass	-	[1.03, 1.59]	[1.03, 1.21]
SNR	-	133	130
Resolution		100,000	100,100
$RV_{\text{bary}}$	$\text{km s}^{-1}$	$[-11.55, -10.89]$	$[-18.84, -18.33]$
$\Delta RV_{\text{bary}}$	$\text{km s}^{-1}$	0.01	0.01
$RV_{\text{planet}}$	$\text{km s}^{-1}$	$[-6.12, 6.09]$	$[-6.18, 6.07]$
$\Delta RV_{\text{planet}}$	$\text{km s}^{-1}$	0.37	0.36

Each CRIRES+ spectral order is projected over three HAWAII-2RG detectors, with the number of orders depending on the spectral band. This allows CRIRES+ to cover each of the *YJHKLM* bands in a single exposure, albeit with gaps between adjacent detectors, and not the whole free spectral range for orders in redder bands. Wavelength calibrations for the *YJHK* bands are achieved through the use of a UNe lamp and a Fabry-Pérot etalon system, which are part of ESO’s daytime calibration routine taken as part of the ESO program 60.A-9051(A).

CRIRES was used for the characterization of exoplanetary atmospheres in transmission or emission even before its upgrade (e.g. Birkby et al. 2013; de Kok et al. 2013; Brogi et al. 2014), with the science continuing post-upgrade given its greater wavelength coverage (e.g. Yan et al. 2023; Lesjak et al. 2023; Ramkumar et al. 2023; Grasser et al. 2024; Parker et al. 2025). The molecular species present in exoplanetary atmospheres at NIR (Near Infra-Red) wavelengths—such as  $\text{H}_2\text{O}$ ,  $\text{CO}_2$ ,  $\text{CO}$ , and  $\text{CH}_4$  to name a few—tend to present as dense forests of absorption features rather than single discrete strong lines, and may typically be detected by cross-correlation with a spectral template.

In our example, we use data from two transits of WASP-107 b, observed as part of Guaranteed Time Observations (GTO) awarded to the CRIRES+ Consortium. The data was already analysed with cross-correlation technique by Boldt-Christmas et al. (2025). The observations were taken using the K2148 wavelength setting, with a series of pre-, in-, and post-transit exposures, and used an ABBA nodding pattern to enable for subtraction of the sky background and detector artifacts. The observations are summarized in Table 3.

The data were reduced using the standard ESO CRIRES+ pipeline (version 2.3.19), available as part of the EsoRex—ESO Recipe Execution—tool (ESO CPL Development Team 2015)<sup>13</sup>. Calibrations were reduced using the EsoRex commands `cr2res_cal_dark`, `cr2res_cal_flat`, and `cr2res_cal_wave`. The science frames were reduced using the command `cr2res_obs_nodding` once for each A/B nodding pair, using the following settings: swath width 800 pixels, oversample 10, extraction height 21 pixels, slit smoothing 0.5, no spectrum smoothing or cosmic hit removal. Blaze correction was performed as part of continuum normalization, using the pipeline-generated blaze functions. We note that TSD does not need correct continuum as such, but homogeneous normalization of all phases helps convergence.

#### 4.2. Data Preparation

For use with the inverse method, the reduced data from both nights needed to be cleaned first and formatted into a spectral datacube with a single uniform wavelength scale of shape  $[N_{\text{phase}}, N_{\text{spec}}, N_{\text{px}}]$  where  $N_{\text{phase}}$  is the total number of phases observed across *both* nights;  $N_{\text{spec}}$  is the number of spectral segments equal to  $N_{\text{order}} \times N_{\text{detector}}$ ; and  $N_{\text{px}}$  is the number of spectral pixels per detector. At each phase, we compute and store the so called ‘timestep information’ describing it, most importantly, the positional and velocity information associated with the system (i.e. barycentric, star, and planet), but also other information like the fraction of the planet currently in transit and the projected  $\mu$  value for computing limb darkening—all of which are necessary for the functioning and convergence of the inverse problem as described above.

Our spectra must be interpolated to a common wavelength scale prior to use which accounts for slight offsets in pixel space between spectra observed in the A and B nodding positions, as well as any drifts during and between

<sup>13</sup> <https://www.eso.org/sci/software/cpl/esorex.html>

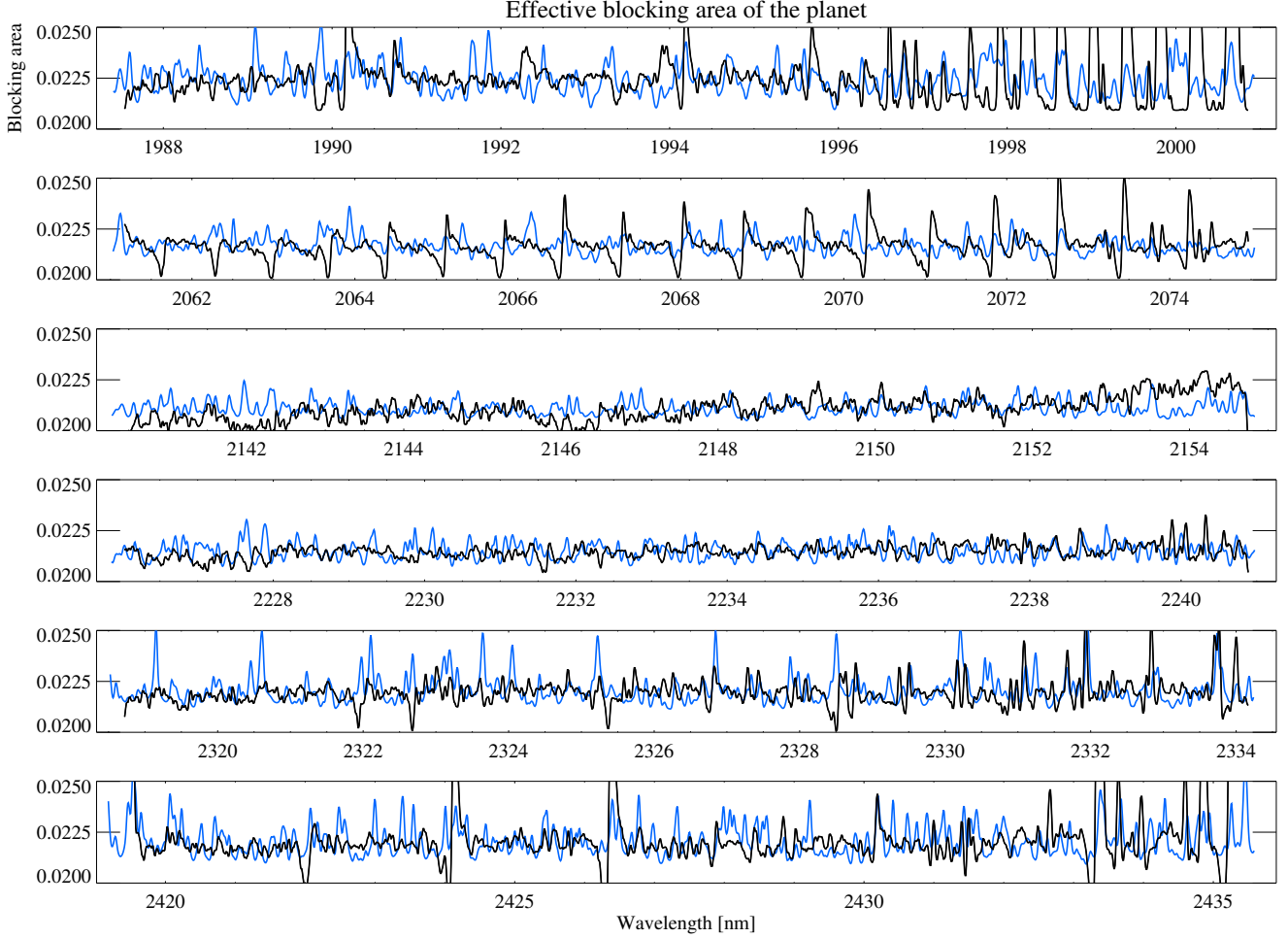


**Figure 8.** Transmission spectrum of WASP-107 b reconstructed with the TSD method using two transits (black). Only the part of the spectrum from the middle detector is presented for clarity, as in Figure 5 and Figure 6. The petitRADTRANS template described in Subsection 3.1.2 (the same as in Figure 6) is shown in blue as a reference. Note that since we do not know what the ‘true’ transmission spectrum of WASP-107 b looks like in reality, this template should be taken as a reference only and not the ground truth as in our simulated observations.

nights. Most of these effects are taken care by the pipeline but some (significant) residuals may remain, particularly when the AO system over-performs in good seeing conditions. We call this effect “super-resolution” (see Appendix 2 in Nortmann et al. 2025). To correct for this effect we homogenized the wavelength solution for all the phases using rich telluric spectrum in order 27 (second order from the top). We then used wavelength morphing to make all exposures for each transit match at this spectral order and computed the transformation between the two transits. The morphing transformation (a second order polynomial in RV) was then applied to all other spectral orders. In the final step, we interpolated the data on a new wavelength grid, common for all the phases and transits, and sigma clipped the data using the `sigma_clip` function from `astropy` to remove a few remaining outliers. The resulting data cube and timestep information table was saved to a FITS file. A more detailed description of this process can be found in Section 3.2 of Boldt-Christmas et al. (2025).

#### 4.3. Results from Real WASP-107 b Data

TSD results on the real data are presented in Figure 8. The regularization parameter for the blocking factor  $P$  was selected with trial-and-error method, where it turns out that anything that keeps regularization functional below 0.2 and above 0.001 of the mean value of  $P$  (around 0.02) is enough to prevent large excursions in the ends of spectral segments and in wavelengths with zero flux due to telluric absorption. We should also point at the correct reconstruction of the mean level of  $P$ —it was not preset.

Here, we have no intention of making a full characterization of the atmosphere of WASP-107 b, which will be the subject of a follow-up paper. Our goal is to give a feeling of TSD’s performance on real data, and this is best done by comparing the analysis of our two real observations with the TSD reconstruction of the simulated data for two transits shown in Figure 6. A numerical assessment of the quality is also given as the bottom number in each cell of Table 2 (either RMS or peak value of the CCF). As one can see, the recovered transmission spectra are different but both do reproduce certain (not necessarily the same) features in the synthetic template, shown in blue. This is not surprising as we do not know if the template actually matches the true transmission spectrum at all wavelengths—a current unknown for *all* exoplanets observed at high spectral resolution. There are also similarities between the two reconstructions: the largest deviations from the template are found in the two top orders and the RMS/CCF pattern follows the simulated two-transit results (not surprisingly, as all the parameters for the simulations, except for the spectra, were taken from the real observations). From those simulations, it is evident that transits are not enough to distinguish between the atmospheric lines of WASP-107 b and strong numerous water lines in the Earth’s atmosphere (see top panel in Figure 3). Noting this limitation, we can conclude that TSD’s performance on the real data is comparable to the reconstruction quality in our numerical experiments and that we may expect significant improvement of the results as additional transits are added. We note that real data contained a few problematic pixels even after thorough tuning of the data reduction pipeline parameters. These included detector defects, only partially removed by nodding pair subtraction, excessively noisy groups of 16 pixels, associated with readout channel of a detector (“random” noise level reaches a few times the value predicted by the Poisson statistics), and super-resolution—all effects that we did not simulate. Despite this, we are happy to report that none of these could derail the application of TSD even though wavelength homogenization was required (see the previous Subsection). Now that we have the confirmation of the ability to recover a transmission spectrum without a priori assumptions about the planetary atmosphere, we can proceed with the atmospheric characterization of hot Jupiters observed in the last few years with CRIRES+ and will aim to present the results in a future series of papers.

## 5. DISCUSSION AND CONCLUSIONS

We have presented a novel method for recovering the high-resolution transmission spectrum (effective blocking area of a planet) from high-resolution transmission spectroscopy observations. The new method is formulated as an inverse problem and it reconstructs three main functions: stellar spectrum, telluric spectrum, and the planetary transmission spectrum. The first two can be verified independently against the observations outside transit or observations of a telluric standard, where they show good agreement with expectations. The main benefit of using TSD is that it does not include any model assumptions about the exoplanetary atmosphere, its chemical composition, pressure-temperature gradients, or vertical stratification. This enables model-based analyses to be done on the resulting transmission spectrum, not unlike classical stellar spectroscopy. TSD can naturally combine multiple transits as it in fact requires more than one transit to work. Ideally, several transits (5-7) with strategically selected barycentric velocities should be combined to obtain the best results, as this enables us to recover planetary features that are “behind” telluric absorption on a given night. Many exoplanets are known to have supersonic winds, and if these are globally coherent, TSD will show their signatures in the recovered line profiles.

### 5.1. TSD Limitations

TSD has number of limitations—some are due to the current implementation, and some are implicit to the method. Here is a non-exhaustive list with possible corrective actions:

- The assumption of constant transmission spectrum for all the phases may not work for some tidally-locked planets. We are considering introducing day- and night-side transmission spectra that will be combined in the model according to the viewing geometry at each phase.
- The relation between stellar flux and specific intensities at a given limb angle  $\mu$  was derived assuming non-rotating star, which excludes Rossiter-McLaughlin effects from our forward model. The assumption can be relaxed by replacing the analytical integration in Equation 5 with numerical integration that incorporates surface motion such as rotation, a simple radial-tangential macroturbulence, and even differential rotation.
- The assumption of constant telluric spectrum throughout a single transit may not be realistic, e.g. when humidity changes significantly. The obvious solution is to split the telluric vector into water and “the rest”, allowing the water part to change smoothly with time in the same way for all wavelengths.

- The uncertainties of the unknown functions were not properly studied in this work. The upcoming Python version of the TSD code will have a Monte Carlo post-processing part dedicated to deriving robust uncertainties.
- The most fundamental limitation of TSD is the need to resolve the change of exoplanet RV during a transit. This is typically not a problem for hot Jupiters, where such changes are measured by a few  $\text{km s}^{-1}$ ; but for Earth analogues we are looking at a few tens of meters per second. For systems with terrestrial planets orbiting an M dwarf (e.g. TRAPPIST-1), the curvature of the orbit increases (smaller orbit) but the stellar mass and size decrease, leading to the lower RV gradient at the middle of the transit. As such, more methodological work will be required to apply TSD-like methods to characterization of true Earth analogues.

### 5.2. Putting TSD in Context with Detrending Methods

Before we conclude, it is worthwhile to more explicitly put an inverse method like TSD in context with the detrending algorithms which remain the field’s method of choice for NIR high-resolution exoplanet transmission spectroscopy. To begin, it is illustrative to consider how each method approaches analysing a transmission spectroscopy dataset, an array of spectra with shape  $[N_{\text{phase}}, N_{\lambda}]$ , the number of exposures and wavelength points respectively. Detrending methods like SYSREM use cross-correlation to boost S/N by collapsing this datacube—the spectral residuals remaining after removing the stellar and telluric signals—in the *wavelength* dimension, preserving radial velocity and time information but losing individual spectral features in the process. TSD, on the other hand, assumes some physical model—in this case Equation 1—describing the combined star–telluric–planet spectra and collapses the datacube instead in the *phase* dimension, preserving spectral information but *assuming* time-independence of the unknown functions. These different solutions of the same problem mean that both methods are complementary to exoplanet transmission spectroscopy, with TSD superior in some ways, and detrending with cross-correlation superior in others. What follows are a few points highlighting some of the advantages of detrending methods:

- These methods work on a single transit with no need to wait for additional transit data, which could take months or even years. In case multiple transits are available, because the combination of transits is done after the cross-correlation step (i.e. in phase–velocity space, not phase–wavelength space as TSD does), one can even combine data taken in different spectral regions or by different instruments.
- If the cross-correlation template is based on extensive previous studies, model assumptions that go into characterization are probably close to reality and can be trusted to produce robust results—at least for high S/N targets such as hot Jupiters with clear atmospheres featuring strong atomic or molecular lines.
- They are mathematically and conceptually simple, extensively developed, tested, and have been successfully used for over 15 years.

However, detrending methods have the following notable disadvantages:

- The core assumption for these methods is that the large phase-to-phase Doppler shift of the exoplanet prevents its signal being detrended unlike its stellar and telluric counterparts. Unfortunately this is not the case in reality, as these techniques also iteratively destroy the planet signal (e.g. Cheverall et al. 2023)—the very thing we are interested in. To date, given the field’s historic focus on hot Jupiters around bright stars, this has not been a limiting factor. However, it will increasingly become an issue as we move towards the study of less-massive planets on longer period orbits around fainter stars.
- The second major limitation is related to the robustness of the results (typically a detection strength in units of S/N) and the lack of method ‘convergence’ (that is the lack of a single and widely agreed upon answer to the question of how many PCA components to remove). We have only a single ‘realization’ of any observation, meaning we have no possibilities to derive statistical uncertainties for CCF peaks or reported S/N detection values for a given molecular species. There are ways to mitigate this weakness, like performing exoplanet injection–recovery tests, but these do not completely resolve the issue. The lack of convergence, on the other hand, adds qualitative, subjective, or ‘as much art as science’ aspects to the methodology which makes it harder for the data to ‘speak for itself’ and challenges easy 1:1 comparisons.

Accordingly, it would be of interest to self-consistently compare these methods, both within a simulated framework and for real observations. This is beyond the scope of our work here, but we have plans to conduct such a comparison in forthcoming work.

### 5.3. Future Prospects

With a functional TSD implementation, we plan to revisit several hot Jupiters, for which a few transits have already been observed with high-resolution spectroscopy. These include the ESO CRIRES+ GTO data and several other archival datasets. We intend to reconstruct the transmission spectra, compare the results with traditional atmospheric retrievals, study atmospheric dynamics, and publish the results for these objects. We are also applying for more observing time to increase the number of transits for systems like WASP-107 b.

In parallel, we plan to continue working on the method, completing the transition to Python, implementing stellar rotation, two-component telluric model (water as one component, all remaining telluric species as the other) and consider separate transmission spectra for the day and night sides of the planet. We will also study the impact of possibly present active regions along the transit path on the robustness of the TSD solution, using our simulation package for this purpose. Finally, we will try pushing TSD to its limit for low-mass planets in anticipation of ELT/ANDES observations.

### ACKNOWLEDGEMENTS

The authors are thankful to the Knut and Alice Wallenberg Foundation for generous support of this project (KAW Scholarship of NP). We also thank Bengt Edvardsson for help with computing MARCS model and specific intensity spectra for WASP-107, and to Thomas Marquart and Alexis Lavail for working with us on optimization of pipeline reduction of CRIRES+ observations. Based on observations collected at the European Organisation for Astronomical Research in the Southern Hemisphere under ESO programmes 108.C-0267(D), 110.C-4127(D), and 0100.C-0750(D). Finally, we want to mention the whole CRIRES+ Consortium that made this project possible.

In this project we used the following software: *Astropy* (Astropy Collaboration et al. 2013), *iPython* (Perez & Granger 2007), *Matplotlib* (Hunter 2007), *NumPy* (Harris et al. 2020), *Pandas* (McKinney 2010; Reback et al. 2020), *SciPy* (Jones et al. 2016; Virtanen et al. 2020), and *PyAstronomy* (Czesla et al. 2019).

### REFERENCES

- Ahrer, E.-M., Gandhi, S., Alderson, L., et al. 2025, *MNRAS*, 540, 2535, doi: [10.1093/mnras/staf819](https://doi.org/10.1093/mnras/staf819)
- Alderson, L., Wakeford, H. R., Alam, M. K., et al. 2023, *Nature*, 614, 664, doi: [10.1038/s41586-022-05591-3](https://doi.org/10.1038/s41586-022-05591-3)
- Allart, R., Bourrier, V., Lovis, C., et al. 2019, *A&A*, 623, A58, doi: [10.1051/0004-6361/201834917](https://doi.org/10.1051/0004-6361/201834917)
- Anderson, D. R., Collier Cameron, A., Delrez, L., et al. 2017, *A&A*, 604, A110, doi: [10.1051/0004-6361/201730439](https://doi.org/10.1051/0004-6361/201730439)
- Aronson, E., & Waldén, P. 2015, *A&A*, 578, A133, doi: [10.1051/0004-6361/201424058](https://doi.org/10.1051/0004-6361/201424058)
- Astropy Collaboration, Robitaille, T. P., Tollerud, E. J., et al. 2013, *A&A*, 558, A33, doi: [10.1051/0004-6361/201322068](https://doi.org/10.1051/0004-6361/201322068)
- Baliunas, S. L., Nesme-Ribes, E., Sokoloff, D., & Soon, W. H. 1996, *ApJ*, 460, 848, doi: [10.1086/177014](https://doi.org/10.1086/177014)
- Bean, J. L., Miller-Ricci Kempton, E., & Homeier, D. 2010, *Nature*, 468, 669, doi: [10.1038/nature09596](https://doi.org/10.1038/nature09596)
- Birkby, J. L., de Kok, R. J., Brogi, M., et al. 2013, *MNRAS: Letters*, 436, L35, doi: [10.1093/mnrasl/slt107](https://doi.org/10.1093/mnrasl/slt107)
- Birkby, J. L., de Kok, R. J., Brogi, M., Schwarz, H., & Snellen, I. A. G. 2017, *AJ*, 153, 138, doi: [10.3847/1538-3881/aa5c87](https://doi.org/10.3847/1538-3881/aa5c87)
- Blain, D., Sánchez-López, A., & Mollière, P. 2024, A formally motivated retrieval framework applied to the high resolution transmission spectrum of HD 189733 b, arXiv. <http://arxiv.org/abs/2402.14001>
- Boldt-Christmas, L., Lesjak, F., Wehrhahn, A., et al. 2024, *A&A*, 683, A244, doi: [10.1051/0004-6361/202347398](https://doi.org/10.1051/0004-6361/202347398)
- Boldt-Christmas, L., Rains, A. D., Piskunov, N., et al. 2025, arXiv e-prints, arXiv:2508.18964, doi: [10.48550/arXiv.2508.18964](https://doi.org/10.48550/arXiv.2508.18964)
- Boucher, A., Darveau-Bernier, A., Pelletier, S., et al. 2021, *The Astronomical Journal*, 162, 233, doi: [10.3847/1538-3881/ac1f8e](https://doi.org/10.3847/1538-3881/ac1f8e)
- Brogi, M., de Kok, R. J., Albrecht, S., et al. 2016, *The Astrophysical Journal*, 817, 106, doi: [10.3847/0004-637X/817/2/106](https://doi.org/10.3847/0004-637X/817/2/106)
- Brogi, M., de Kok, R. J., Birkby, J. L., Schwarz, H., & Snellen, I. a. G. 2014, *A&A*, 565, A124, doi: [10.1051/0004-6361/201423537](https://doi.org/10.1051/0004-6361/201423537)
- Brogi, M., Line, M., Bean, J., Désert, J. M., & Schwarz, H. 2017, *ApJL*, 839, L2, doi: [10.3847/2041-8213/aa6933](https://doi.org/10.3847/2041-8213/aa6933)
- Brogi, M., & Line, M. R. 2019, *AJ*, 157, 114, doi: [10.3847/1538-3881/aafdd3](https://doi.org/10.3847/1538-3881/aafdd3)
- Brogi, M., Emeka-Okafor, V., Line, M. R., et al. 2023, *The Astronomical Journal*, 165, 91, doi: [10.3847/1538-3881/acaf5c](https://doi.org/10.3847/1538-3881/acaf5c)

- Charbonneau, D., Brown, T. M., Noyes, R. W., & Gilliland, R. L. 2002, *ApJ*, 568, 377, doi: [10.1086/338770](https://doi.org/10.1086/338770)
- Cheverall, C. J., Madhusudhan, N., & Holmberg, M. 2023, *MNRAS*, 522, 661, doi: [10.1093/mnras/stad648](https://doi.org/10.1093/mnras/stad648)
- Claret, A. 2000, *A&A*, 363, 1081
- Cont, D., Nortmann, L., Yan, F., et al. 2024, *Astronomy and Astrophysics*, 688, A206, doi: [10.1051/0004-6361/202450064](https://doi.org/10.1051/0004-6361/202450064)
- Cowan, N. B., Machalek, P., Croll, B., et al. 2012, *ApJ*, 747, 82, doi: [10.1088/0004-637X/747/1/82](https://doi.org/10.1088/0004-637X/747/1/82)
- Czesla, S., Schröter, S., Schneider, C. P., et al. 2019, *PyA: Python astronomy-related packages*. <http://ascl.net/1906.010>
- de Kok, R. J., Brogi, M., Snellen, I. a. G., et al. 2013, *A&A*, 554, A82, doi: [10.1051/0004-6361/201321381](https://doi.org/10.1051/0004-6361/201321381)
- Deming, D., Wilkins, A., McCullough, P., et al. 2013, *ApJ*, 774, 95, doi: [10.1088/0004-637X/774/2/95](https://doi.org/10.1088/0004-637X/774/2/95)
- Désert, J.-M., Lecavelier des Etangs, A., Hébrard, G., et al. 2009, *ApJ*, 699, 478, doi: [10.1088/0004-637X/699/1/478](https://doi.org/10.1088/0004-637X/699/1/478)
- Dorn, R. J., Bristow, P., Smoker, J. V., et al. 2023, *A&A*, 671, A24, doi: [10.1051/0004-6361/202245217](https://doi.org/10.1051/0004-6361/202245217)
- Dyrek, A., Min, M., Decin, L., et al. 2024, *Nature*, 625, 51, doi: [10.1038/s41586-023-06849-0](https://doi.org/10.1038/s41586-023-06849-0)
- ESO CPL Development Team. 2015, *Astrophysics Source Code Library*, ascl:1504.003. <https://ui.adsabs.harvard.edu/abs/2015ascl.soft04003E>
- Esparza-Borges, E., Oshagh, M., Casasayas-Barris, N., et al. 2022, *A&A*, 657, A23, doi: [10.1051/0004-6361/202141826](https://doi.org/10.1051/0004-6361/202141826)
- Gandhi, S., Brogi, M., Yurchenko, S. N., et al. 2020, *MNRAS*, 495, 224, doi: [10.1093/mnras/staa981](https://doi.org/10.1093/mnras/staa981)
- Gandhi, S., Kesseli, A., Zhang, Y., et al. 2023, *The Astronomical Journal*, 165, 242, doi: [10.3847/1538-3881/accd65](https://doi.org/10.3847/1538-3881/accd65)
- Grasser, N., Snellen, I. A. G., Landman, R., Picos, D. G., & Gandhi, S. 2024, *A&A*, 688, A191, doi: [10.1051/0004-6361/202449932](https://doi.org/10.1051/0004-6361/202449932)
- Grevesse, N., Asplund, M., & Sauval, A. J. 2007, *SSRv*, 130, 105, doi: [10.1007/s11214-007-9173-7](https://doi.org/10.1007/s11214-007-9173-7)
- Guilluy, G., D’Arpa, M. C., Bonomo, A. S., et al. 2024, *A&A*, 686, A83, doi: [10.1051/0004-6361/202348997](https://doi.org/10.1051/0004-6361/202348997)
- Gustafsson, B., Edvardsson, B., Eriksson, K., et al. 2008, *A&A*, 486, 951, doi: [10.1051/0004-6361:200809724](https://doi.org/10.1051/0004-6361:200809724)
- Gustafsson, B., Edvardsson, B., Eriksson, K., et al. 2008, *A&A*, 486, 951, doi: [10.1051/0004-6361:200809724](https://doi.org/10.1051/0004-6361:200809724)
- Harris, C. R., Millman, K. J., van der Walt, S. J., et al. 2020, *Nature*, 585, 357, doi: [10.1038/s41586-020-2649-2](https://doi.org/10.1038/s41586-020-2649-2)
- Hoeijmakers, H. J., de Kok, R. J., Snellen, I. A. G., et al. 2015, *A&A*, 575, A20, doi: [10.1051/0004-6361/201424794](https://doi.org/10.1051/0004-6361/201424794)
- Hunter, J. D. 2007, *Computing in Science Engineering*, 9, 90, doi: [10.1109/MCSE.2007.55](https://doi.org/10.1109/MCSE.2007.55)
- Jones, E., Oliphant, T., & Peterson, P. 2016, *SciPy: Open source scientific tools for Python*, 2001 (scipy.org)
- Kaeufl, H.-U., Ballester, P., Biereichel, P., et al. 2004, in *Ground-based Instrumentation for Astronomy*, Vol. 5492 (SPIE), 1218–1227, doi: [10.1117/12.551480](https://doi.org/10.1117/12.551480)
- Kausch, W., Noll, S., Smette, A., et al. 2015, *A&A*, 576, A78, doi: [10.1051/0004-6361/201423909](https://doi.org/10.1051/0004-6361/201423909)
- Kirk, J., Alam, M. K., López-Morales, M., & Zeng, L. 2020, *AJ*, 159, 115, doi: [10.3847/1538-3881/ab6e66](https://doi.org/10.3847/1538-3881/ab6e66)
- Knutson, H. A., Madhusudhan, N., Cowan, N. B., et al. 2011, *ApJ*, 735, 27, doi: [10.1088/0004-637X/735/1/27](https://doi.org/10.1088/0004-637X/735/1/27)
- Kostogryz, N. M., Shapiro, A. I., Witzke, V., et al. 2024, *Nature Astronomy*, 8, 929, doi: [10.1038/s41550-024-02252-5](https://doi.org/10.1038/s41550-024-02252-5)
- Kreidberg, L., Line, M. R., Thorngren, D., Morley, C. V., & Stevenson, K. B. 2018, *ApJL*, 858, L6, doi: [10.3847/2041-8213/aabf3e](https://doi.org/10.3847/2041-8213/aabf3e)
- Kreidberg, L., Line, M. R., Bean, J. L., et al. 2015, *ApJ*, 814, 66, doi: [10.1088/0004-637X/814/1/66](https://doi.org/10.1088/0004-637X/814/1/66)
- Lendl, M., Delrez, L., Gillon, M., et al. 2016, *A&A*, 587, A67, doi: [10.1051/0004-6361/201527594](https://doi.org/10.1051/0004-6361/201527594)
- Lesjak, F., Nortmann, L., Yan, F., et al. 2023, *A&A*, 678, A23, doi: [10.1051/0004-6361/202347151](https://doi.org/10.1051/0004-6361/202347151)
- Magic, Z., Chiavassa, A., Collet, R., & Asplund, M. 2015, *A&A*, 573, A90, doi: [10.1051/0004-6361/201423804](https://doi.org/10.1051/0004-6361/201423804)
- Maguire, C., Sedaghati, E., Gibson, N. P., Smette, A., & Pino, L. 2024, *A&A*, 692, A8, doi: [10.1051/0004-6361/202451784](https://doi.org/10.1051/0004-6361/202451784)
- Mayor, M., & Queloz, D. 1995, *Nature*, 378, 355, doi: [10.1038/378355a0](https://doi.org/10.1038/378355a0)
- McKinney, W. 2010, in *Proceedings of the 9th Python in Science Conference*, 51–56, doi: [10.25080/Majora-92bf1922-00a](https://doi.org/10.25080/Majora-92bf1922-00a)
- McLaughlin, D. B. 1924, *ApJ*, 60, 22, doi: [10.1086/142826](https://doi.org/10.1086/142826)
- Meech, A., Aigrain, S., Brogi, M., & Birkby, J. L. 2022, *MNRAS*, 512, 2604, doi: [10.1093/mnras/stac662](https://doi.org/10.1093/mnras/stac662)
- Mittag, M., Schmitt, J. H. M. M., & Schröder, K. P. 2018, *A&A*, 618, A48, doi: [10.1051/0004-6361/201833498](https://doi.org/10.1051/0004-6361/201833498)
- Močnik, T., Hellier, C., Anderson, D. R., Clark, B. J. M., & Southworth, J. 2017, *MNRAS*, 469, 1622, doi: [10.1093/mnras/stx972](https://doi.org/10.1093/mnras/stx972)
- Mollière, P., Wardenier, J. P., van Boekel, R., et al. 2019, *A&A*, 627, A67, doi: [10.1051/0004-6361/201935470](https://doi.org/10.1051/0004-6361/201935470)
- Nortmann, L., Lesjak, F., Yan, F., et al. 2025, *A&A*, 693, A213, doi: [10.1051/0004-6361/202450438](https://doi.org/10.1051/0004-6361/202450438)
- Parker, L. T., Mendonça, J. M., Diamond-Lowe, H., et al. 2025, *MNRAS*, 538, 3263, doi: [10.1093/mnras/staf469](https://doi.org/10.1093/mnras/staf469)
- Paufique, J., Biereichel, P., Donaldson, R., et al. 2004, in *Advancements in Adaptive Optics*, Vol. 5490 (SPIE), 216–227, doi: [10.1117/12.551675](https://doi.org/10.1117/12.551675)

- Perez, F., & Granger, B. E. 2007, *Computing in Science Engineering*, 9, 21, doi: [10.1109/MCSE.2007.53](https://doi.org/10.1109/MCSE.2007.53)
- Piaulet, C., Benneke, B., Rubenzahl, R. A., et al. 2021, *AJ*, 161, 70, doi: [10.3847/1538-3881/abcd3c](https://doi.org/10.3847/1538-3881/abcd3c)
- Piskunov, N., & Valenti, J. A. 2017, *A&A*, 597, A16, doi: [10.1051/0004-6361/201629124](https://doi.org/10.1051/0004-6361/201629124)
- Pollacco, D. L., Skillen, I., Collier Cameron, A., et al. 2006, *PASP*, 118, 1407, doi: [10.1086/508556](https://doi.org/10.1086/508556)
- Polyansky, O. L., Kyuberis, A. A., Zobov, N. F., et al. 2018, *MNRAS*, 480, 2597, doi: [10.1093/mnras/sty1877](https://doi.org/10.1093/mnras/sty1877)
- Pont, F., Knutson, H., Gilliland, R. L., Moutou, C., & Charbonneau, D. 2008, *MNRAS*, 385, 109, doi: [10.1111/j.1365-2966.2008.12852.x](https://doi.org/10.1111/j.1365-2966.2008.12852.x)
- Prinot, B., Hoeijmakers, H. J., Kitzmann, D., et al. 2022, *Nature Astronomy*, 6, 449, doi: [10.1038/s41550-021-01581-z](https://doi.org/10.1038/s41550-021-01581-z)
- Ramkumar, S., Gibson, N. P., Nugroho, S. K., Maguire, C., & Fortune, M. 2023, High-resolution emission spectroscopy retrievals of MASCARA-1b with CRIRES+, arXiv, doi: [10.48550/arXiv.2308.07157](https://doi.org/10.48550/arXiv.2308.07157)
- Reback, J., McKinney, W., jbrockmendel, et al. 2020, *pandas-dev/pandas: Pandas 1.1.0*, Zenodo, doi: [10.5281/zenodo.3964380](https://doi.org/10.5281/zenodo.3964380)
- Rossiter, R. A. 1924, *ApJ*, 60, 15, doi: [10.1086/142825](https://doi.org/10.1086/142825)
- Rothman, L. S., Gordon, I. E., Barber, R. J., et al. 2010, *JQSRT*, 111, 2139, doi: [10.1016/j.jqsrt.2010.05.001](https://doi.org/10.1016/j.jqsrt.2010.05.001)
- Rubenzahl, R. A., Dai, F., Howard, A. W., et al. 2021, *AJ*, 161, 119, doi: [10.3847/1538-3881/abd177](https://doi.org/10.3847/1538-3881/abd177)
- Rustamkulov, Z., Sing, D. K., Mukherjee, S., et al. 2023, *Nature*, 614, 659, doi: [10.1038/s41586-022-05677-y](https://doi.org/10.1038/s41586-022-05677-y)
- Savel, A. B., Bedell, M., Kempton, E. M. R., et al. 2025, *AJ*, 169, 135, doi: [10.3847/1538-3881/ada27e](https://doi.org/10.3847/1538-3881/ada27e)
- Sedaghati, E., Boffin, H. M. J., MacDonald, R. J., et al. 2017, *Nature*, 549, 238, doi: [10.1038/nature23651](https://doi.org/10.1038/nature23651)
- Seidel, J. V., Ehrenreich, D., Allart, R., et al. 2021, *Astronomy and Astrophysics*, 653, A73, doi: [10.1051/0004-6361/202140569](https://doi.org/10.1051/0004-6361/202140569)
- Seidel, J. V., Prinot, B., Pino, L., et al. 2025, *Nature*, 639, 902, doi: [10.1038/s41586-025-08664-1](https://doi.org/10.1038/s41586-025-08664-1)
- Sing, D. K., Vidal-Madjar, A., Désert, J. M., Lecavelier des Etangs, A., & Ballester, G. 2008, *The Astrophysical Journal*, 686, 658, doi: [10.1086/590075](https://doi.org/10.1086/590075)
- Sing, D. K., Désert, J. M., Fortney, J. J., et al. 2011, *A&A*, 527, A73, doi: [10.1051/0004-6361/201015579](https://doi.org/10.1051/0004-6361/201015579)
- Sing, D. K., Rustamkulov, Z., Thorngren, D. P., et al. 2024, *Nature*, 630, 831, doi: [10.1038/s41586-024-07395-z](https://doi.org/10.1038/s41586-024-07395-z)
- Skrutskie, M. F., Cutri, R. M., Stiening, R., et al. 2006, *AJ*, 131, 1163, doi: [10.1086/498708](https://doi.org/10.1086/498708)
- Smette, A., Sana, H., Noll, S., et al. 2015, *A&A*, 576, A77, doi: [10.1051/0004-6361/201423932](https://doi.org/10.1051/0004-6361/201423932)
- Smith, P. C. B., Line, M. R., Bean, J. L., et al. 2024, *The Astronomical Journal*, 167, 110, doi: [10.3847/1538-3881/ad17bf](https://doi.org/10.3847/1538-3881/ad17bf)
- Snellen, I. A. G. 2025, *ARA&A*, 63, 83, doi: [10.1146/annurev-astro-052622-031342](https://doi.org/10.1146/annurev-astro-052622-031342)
- Snellen, I. A. G., de Kok, R. J., de Mooij, E. J. W., & Albrecht, S. 2010, *Nature*, 465, 1049, doi: [10.1038/nature09111](https://doi.org/10.1038/nature09111)
- Snellen, I. A. G., de Kok, R. J., de Mooij, E. J. W., & Albrecht, S. 2010, *Nature*, 465, 1049, doi: [10.1038/nature09111](https://doi.org/10.1038/nature09111)
- Spake, J. J., Oklopčić, A., & Hillenbrand, L. A. 2021, *AJ*, 162, 284, doi: [10.3847/1538-3881/ac178a](https://doi.org/10.3847/1538-3881/ac178a)
- Spake, J. J., Sing, D. K., Evans, T. M., et al. 2018, *Nature*, 557, 68, doi: [10.1038/s41586-018-0067-5](https://doi.org/10.1038/s41586-018-0067-5)
- Stelzer, B., Damasso, M., Scholz, A., & Matt, S. P. 2016, *MNRAS*, 463, 1844, doi: [10.1093/mnras/stw1936](https://doi.org/10.1093/mnras/stw1936)
- Stempels, H. C., Piskunov, N., & Barklem, P. S. 2001, in *Astronomical Society of the Pacific Conference Series*, Vol. 223, 11th Cambridge Workshop on Cool Stars, Stellar Systems and the Sun, ed. R. J. Garcia Lopez, R. Rebolo, & M. R. Zapaterio Osorio, 878
- Tamuz, O., Mazeh, T., & Zucker, S. 2005, *MNRAS*, 356, 1466, doi: [10.1111/j.1365-2966.2004.08585.x](https://doi.org/10.1111/j.1365-2966.2004.08585.x)
- Tikhonov, A. N., Goncharsky, A. V., Stepanov, V. V., & Yagola, A. G. 1995, *Numerical Methods for the Solution of Ill-Posed Problems* (Springer Netherlands), doi: [10.1007/978-94-015-8480-7](https://doi.org/10.1007/978-94-015-8480-7)
- Tinetti, G., Vidal-Madjar, A., Liang, M.-C., et al. 2007, *Nature*, 448, 169, doi: [10.1038/nature06002](https://doi.org/10.1038/nature06002)
- Tsai, S.-M., Lee, E. K. H., Powell, D., et al. 2023, *Nature*, 617, 483, doi: [10.1038/s41586-023-05902-2](https://doi.org/10.1038/s41586-023-05902-2)
- Vallenari, A., Brown, A. G. A., Prusti, T., et al. 2023, *A&A*, 674, A1, doi: [10.1051/0004-6361/202243940](https://doi.org/10.1051/0004-6361/202243940)
- Vidal-Madjar, A., Désert, J. M., Lecavelier des Etangs, A., et al. 2004, *ApJL*, 604, L69, doi: [10.1086/383347](https://doi.org/10.1086/383347)
- Virtanen, P., Gommers, R., Oliphant, T. E., et al. 2020, *Nature Methods*, 17, 261, doi: [10.1038/s41592-019-0686-2](https://doi.org/10.1038/s41592-019-0686-2)
- Wakeford, H. R., Sing, D. K., Kataria, T., et al. 2017, *Science*, 356, 628, doi: [10.1126/science.aah4668](https://doi.org/10.1126/science.aah4668)
- Watson, C. A., de Mooij, E. J. W., Steeghs, D., et al. 2019, *MNRAS*, 490, 1991, doi: [10.1093/mnras/stz2679](https://doi.org/10.1093/mnras/stz2679)
- Welbanks, L., Bell, T. J., Beatty, T. G., et al. 2024, *Nature*, 630, 836, doi: [10.1038/s41586-024-07514-w](https://doi.org/10.1038/s41586-024-07514-w)
- Yan, F., Nortmann, L., Reiners, A., et al. 2023, *A&A*, 672, A107, doi: [10.1051/0004-6361/202245371](https://doi.org/10.1051/0004-6361/202245371)
- Yurchenko, S. N., Barber, R. J., & Tennyson, J. 2011, *MNRAS*, 413, 1828, doi: [10.1111/j.1365-2966.2011.18261.x](https://doi.org/10.1111/j.1365-2966.2011.18261.x)